Chemical Engineering Journal 534 (2026) 174848

Contents lists available at ScienceDirect

Chemical Engineering Journal

journal homepage: www.elsevier.com/locate/cej

Effect of carbonyl group position on redox-active anthraquinone–, phenanthrenequinone–, and benzil–linked hexaazatrinaphthalene conjugated microporous polymers for supercapacitor electrodes

Aya Farouk Farghal [a,b], Tharwat H. Mansoure [a,b], Mohamed Gamal Mohamed [a,b], Ahmed A.K. Mohammed [b], Shiao-Wei Kuo [a,c,*]

[a] Department of Materials and Optoelectronic Science, Center for Functional Polymers and Supramolecular Materials, National Sun Yat-Sen University, Kaohsiung, 804, Taiwan
[b] Department of Chemistry, Faculty of Science, Assiut University, Assiut, 71515, Egypt
[c] Department of Medicinal and Applied Chemistry, Kaohsiung Medical University, Kaohsiung, 807, Taiwan

ARTICLE INFO

Keywords:
Carbonyl-position engineering
Conjugated microporous polymers (CMPs)
Supercapacitors
Anthraquinone
Redox active centers

ABSTRACT

Developing advanced organic electrode materials (OEMs) is vital for the progress of next-generation energy storage systems. Among them, redox-active conjugated microporous polymers (CMPs) stand out as promising candidates for supercapacitors (SCs) because of their tunable electronic structures and intrinsic porosity. Herein, we report anthraquinone (AQ)-, phenanthrenequinone (PQ)-, and benzil (DPED)-linked hexaazatrinaphthalene-based CMPs–AQ-HATN, PQ-HATN, and DPED-HATN–constructed via Suzuki–Miyaura coupling. These frameworks integrate a nitrogen-rich HATN core with carbonyl moieties featuring systematically varied conjugation geometries and carbonyl positions. Benefiting from high densities of redox-active sites, extended π-conjugation, and hierarchical microporosity, the CMPs exhibit large surface areas, tunable pores, high capacitance, and long-term durability. In a three-electrode configuration, the AQ-HATN CMP achieves a specific capacitance of 543 ± 4.1 F g^{-1} at 0.5 A g^{-1}, demonstrating remarkable electrochemical stability with 96.2% retention after 10,000 consecutive cycles at 10 A g^{-1}. A symmetric AQ-HATN CMP//AQ-HATN CMP device achieves a total specific capacitance of 174.07 ± 1.3 F g^{-1} at 0.1 A g^{-1} (328.14 ± 2.6 F g^{-1} per electrode), an energy density of 34.8 ± 0.3 Wh Kg^{-1} at 60 W Kg^{-1} (69.62 ± 0.6 Wh Kg^{-1} at 120 W Kg^{-1} per electrode), and nearly 100% Coulombic efficiency at 1 A g^{-1} after 10,000 cycles. Structurally, AQ-HATN features a *para*-diketone arrangement promoting planar geometry and extended π-conjugation, PQ-HATN has a *peri*-diketone arrangement that distorts planarity, and DPED-HATN exhibits a *vicinal*-diketone arrangement limiting electronic delocalization. This study demonstrates that precise carbonyl-position engineering and linker conjugation enable rational molecular design for high-performance organic SCs electrodes.

1. Introduction

The ever-increasing worldwide need for renewable and environmentally friendly energy sources has placed immense emphasis on developing efficient energy storage technologies capable of complementing intermittent renewable sources like solar and wind [1–4]. Among the various energy storage systems, SCs have emerged as a highly prominent viable alternative ascribed to their rapid charge–discharge rates, exceptional cycling stability, and superior power density compared with conventional batteries [5–8]. Their fast surface-controlled redox processes enable quick energy delivery and remarkable durability, making them indispensable for hybrid electric vehicles, portable electronics, and large-scale renewable energy integration [9–12]. Despite these advantages, the relatively low energy density of supercapacitors remains a critical limitation. This limitation is primarily associated with the restricted charge-storage mechanisms of conventional electrode materials. Consequently, the development of advanced electrode materials with high redox-site density, optimized pore architecture, and efficient charge-transport pathways has become a central strategy for enhancing supercapacitor energy density while maintaining

* Corresponding author at: Department of Materials and Optoelectronic Science, Center for Functional Polymers and Supramolecular Materials, National Sun Yat-Sen University, Kaohsiung, 804, Taiwan.
E-mail address: kuosw@faculty.nsysu.edu.tw (S.-W. Kuo).

https://doi.org/10.1016/j.cej.2026.174848
Received 2 November 2025; Received in revised form 4 February 2026; Accepted 2 March 2026
Available online 4 March 2026

high power performance and long cycling stability. Conjugated microporous polymers (CMPs) have recently attracted considerable attention as a novel subclass of porous organic frameworks (POFs) for high-performance SC electrodes [13–15], batteries [16–18], and fuel cells [19], as well as for other applications such as CO_2 capture [20], gas separation [21], photocatalytic hydrogen evolution [22,23], hydrogen peroxide generation [22], heterogeneous catalysis [24,25], drug delivery [26], sensing [27], and optoelectronics [28]. CMPs feature extended π-conjugated backbones combined with intrinsic microporosity, resulting in highly accessible surface areas, substantial pore volumes, ultralow density, and remarkable chemical and thermal robustness [15–17]. These structural features promote rapid ion diffusion and facile electrolyte penetration–key factors for improving supercapacitor performance. Moreover, the incorporation of redox-active building blocks and heteroatom doping within CMP frameworks introduces additional faradaic sites, enabling pseudocapacitive behavior with enhanced charge-storage capacity and cycling durability [5,6,29]. Another major advantage of CMPs is their high tunability: by varying monomer composition and polymerization strategy, it is possible to tailor pore architecture, surface chemistry, and electronic properties precisely [28–30]. This molecular design flexibility renders CMPs an excellent platform for engineering next-generation energy-storage materials with optimized charge transport and ion accessibility. Various synthetic methodologies have been developed for CMPs, including cyclotrimerization, phenazine ring fusion, oxidative polymerization, and Schiff-base condensation [15,17,30,31]. In addition, cross-coupling techniques such as Sonogashira–Hagihara, Heck, Buchwald-Hartwig, Yamamoto, and Suzuki–Miyaura coupling [19,22,30,31] have been extensively used to build highly conjugated frameworks with diverse structures and tunable properties, thereby broadening their applicability in energy-storage systems [31]. Such modular synthetic control enables systematic tuning of electronic structure and redox activity, offering a robust molecular toolkit for performance optimization in supercapacitors [31].

Among various redox-active motifs, quinone- and carbonyl-based molecules have been widely recognized for their highly reversible multi-electron redox reactions, structural stability, and environmental compatibility [13,29,32–39]. Their ability to undergo fast and reversible redox transitions between carbonyl (C=O) and hydroxyl (C–OH) states enables efficient charge transfer and energy storage [13]. However, quinone-based materials often suffer from limited conductivity and dissolution in electrolytes, which hinder rate capability and cycling stability [13,40,41]. Integrating quinone derivatives into conjugated polymeric frameworks has been shown to significantly improve their electrochemical reversibility, charge transport, and structural integrity [9,10,42–47]. In particular, the position and local electronic environment of carbonyl groups play a crucial role in determining orbital delocalization, redox potential, and ion accessibility–yet systematic investigations on how carbonyl position engineering influences redox activity and electronic properties within CMPs remain scarce. Hexaazatrinaphthalene (HATN)–a nitrogen-rich polycyclic aromatic compound–has recently emerged as a powerful electron-deficient building unit for constructing π-conjugated redox-active frameworks [7,14,15,48–52]. Its planar, rigid structure enables strong π–π stacking and efficient charge transport, while its high electron affinity and multiple nitrogen sites facilitate favorable interactions with electrolyte ions, promoting rapid redox kinetics. Integrating carbonyl-containing moieties with HATN units into donor–acceptor (D–A)-type CMPs thus represents a compelling strategy to modulate electronic energy levels, enhance charge-transfer efficiency, and achieve highly reversible pseudocapacitive behavior [48–52]. Although carbonyl- and quinone-containing units have been incorporated into conjugated polymers or HATN-based frameworks, the deliberate regulation of *para*-, *peri*-, and *vicinal*-diketone carbonyl positions within CMP backbones–and its impact on framework packing, electronic delocalization, and redox behavior has not been systematically investigated. In particular, how distinct carbonyl geometries impose different steric and electronic constraints in HATN-based CMPs remains largely unexplored.

In this work, we systematically engineered the position and nature of carbonyl groups within a series of redox-active HATN-based CMPs to investigate their influence on electronic structure, porosity architecture, and electrochemical performances. Three polymers–AQ-HATN, PQ-HATN, and DPED-HATN–were synthesized via Suzuki–Miyaura coupling using 2,8,14-tribromodiquinoxalino[2,3-a:2′,3′-c]phenazine (HATN-3Br) as the electron-donating core and three distinct carbonyl-based linkers: 2,6-dibromoanthraquinone (AQ-2Br), 3,6-dibromophenanthrene-9,10-dione (PQ-2Br), and 1,2-bis(4-bromophenyl)ethane-1,2-dione (DPED-2Br), respectively. Nitrogen adsorption and non-linear density functional theory (NLDFT) analyses confirm the presence of a hierarchical micro–mesoporous network in all CMPs, with AQ-HATN displaying the most favorable balance of micropores and mesopores for rapid electrolyte diffusion. DFT calculations further reveal that AQ-HATN CMP possesses the most delocalized HOMO–LUMO orbitals, promoting efficient electron transport, whereas DPED-HATN CMP exhibits more localized frontier orbitals, limiting charge mobility. As a result, symmetric device (AQ-HATN CMP//AQ-HATN CMP) achieves a total capacitance of 174.07 ± 1.3 F g^{-1} (328.14 ± 2.6 F g^{-1} per electrode) at 0.1 A g^{-1}, along with an energy density of 34.8 ± 0.3 Wh Kg^{-1} (69.62 ± 0.6 Wh Kg^{-1} per electrode) at a power density of 60 W Kg^{-1} (120 W Kg^{-1} per electrode), combined with 100% capacitance retention and Coulombic efficiency over 10,000 cycles at 1 A g^{-1}. These results demonstrate that optimal supercapacitor performance arises from the synergistic interplay of conjugation geometry, molecular planarity, orbital delocalization, and hierarchical porosity, highlighting the critical role of carbonyl positions and linker conjugation in modulating CMP electrochemical performance.

2. Experimental section

2.1. Resources

All reagents are used as it is without any extra purification, 4-bromobenzene-1,2-diamine (4Br-BZ-2NH_2) ($C_6H_7BrN_2$, BLDpharm, 98%), glacial acetic acid (AcOH, Fluka, ≥99.8%), Tetrakis(triphenylphosphine)palladium(0) ($Pd(PPh_3)_4$, thermo scientific, 99.0%), 1,4-phenylenediboronic acid (PDBA, TCI America, 99%), potassium carbonate (K_2CO_3, SHOWA, 99.0%), fuming nitric acid (HNO_3, union chemical works ltd, >98.0%), hydrochloric acid (HCl, Fluka, ≥37%), DPED-2Br (thermo fisher scientific, 97%), cyclohexanone octahydrate (97%), phenanthrene-9,10-dione (PQ, 95%), tert-butyl nitrite ($(CH_3)_3CONO$, 90%), Copper(II) bromide ($CuBr_2$, 99%), 2,6-diaminoanthracene-9,10-dione (AQ-2NH_2, 97%), acetonitrile (MeCN, ≥99.9%), dibenzoyl peroxide ($(C_6H_5CO)_2O_2$, 75%), nitrobenzene ($C_6H_5NO_2$, ≥99.0%), bromine (Br_2, 98.0–102.0%), finally solvents like Dimethylformamide (DMF), Tetrahydrofuran (THF), acetone, and methanol (MeOH) all were bought from Sigma-Aldrich.

2.2. Synthesis of HATN-3Br

As shown in **scheme S1**, (2 g, 6.41 mmol) of cyclohexanone octahydrate and (3.5 g, 18.72 mmol) of 4Br-BZ-2NH_2 were transferred to a two-necked flask under N_2 atmosphere and constant stirring. After that, 120 mL of AcOH was added drop by drop into the reaction solution, which was subsequently then refluxed at 100 °C overnight. The resulting crude product was collected and thoroughly washed with deionized H_2O and EtOH. The yellow-green powder that resulted was subsequently exposed to oxidation using 60 mL of 40 wt% nitric acid with constant stirring and refluxing at 130 °C for 6 h. Following the reaction's completion, water and methanol were used to wash the finished product. Then drying at 70 °C overnight to give the yellow powder of HATN-3Br. FT-IR (**Fig. S1**): aromatic C—H (3067 cm^{-1}), C=N (1605 cm^{-1}), 1483 cm^{-1} (C=C). HR ES-MS (*m/z*): calcd for ($C_{24}H_9Br_3N_6$), 621.09;

found, 621.84 (**Fig. S2**).

2.3. Synthesis of AQ-2Br

AQ-2Br was synthesized as previously reported in the literature [53] and illustrated in **Scheme S2**, in which, into a dry reaction flask, 18 mL of tert-butyl nitrite was incrementally added into a blend of $CuBr_2$ (10.56 g, 47.25 mmol) and AQ-2NH_2 (4.5 g, 18.9 mmol) dissolved in MeCN (150 mL). Following a 24 h reflux period at 75 °C, 300 mL of 6 M HCl was gradually added. AQ-2Br (3.51 g, 78% yield) was finally obtained by successively washing the filtered yield of brown powder with water, MeCN, and MeOH. FT-IR (**Fig. S3**): 3101 cm^{-1} (C—H aromatic), 1677 cm^{-1} (C=O), 1583 cm^{-1} (C=C). ^{1}H NMR (**Fig. S4**): 8.66, 7.92, 7.757. ^{13}C NMR (125 MHz, $CDCl_3$, δ, **Fig. S5**): 179.66–127.60.

2.4. Synthesis of PQ-2Br

In addition, we synthesized PQ-2Br as previously reported, with some modifications [6], Into a round flask, a mixture of (6 g, 28.81 mmol) of PQ and (0.768 g, 3.17 mmol) of dibenzoyl peroxide was dissolved in 75 mL of nitrobenzene. After that, 4.1 mL (80.1 mmol) of Br2 was added to the whole mixture, which was then refluxed at 100 °C for 17 h. The resulting powder was washed with hexane and water to obtain PQ-2Br (9.48 g) as a yellow powder (**Scheme S3**). FT-IR (**Fig. S6**): 3101 cm^{-1} (C—H aromatic), 1677 cm^{-1} (C=O), 1583 cm^{-1} (C=C). ^{1}H NMR (**Fig. S7**): 8.66, 7.92, 7.757.

2.5. Synthesis of AQ-HATN, PQ-HATN, and DPED-HATN CMPs

AQ-HATN CMP was synthesized as a brown powder (yield: 95%, **Scheme S4**) using Suzuki coupling reaction as the following: A combination of (0.2 g, 0.322 mmol) of HATN-3Br, (0.177 g, 0.483 mmol) of AQ-2Br, (0.1601 g, 0.966 mmol) of PDBA, (0.356 g, 2.58 mmol) of K_2CO_3 and (0.055 g, 0.043 mmol) of ($Pd(PPh_3)_4$ were transferred to two-necked round flask. Afterward, 30 mL of DMF and 10 mL of H_2O were put into the round flask, then the whole mixture was degassed three times through freeze pump and thaw, and then was refluxed under nitrogen at 120 °C for 3 days. Once the reaction is completed and cooled to 25 °C, the product solid was filtered using a vacuum pump and washed well with DMF, H_2O, THF, MeOH, and acetone, then dried at 70 °C for 12 h to obtain AQ-HATN CMP. For the synthesis of PQ-HATN, and DPED-HATN CMPs, we used the same procedure as AQ-HATN CMP, whereas we replaced AQ-2Br with (0.1768 g, 0.483 mmol) of PQ-2Br to provide a black powder of PQ-HATN CMP (yield: 85%, **Scheme S5**) and also replaced it with (0.1778 g, 0.483 mmol) of DPED-2Br to offer a light brown of DPED-HATN CMP (yield: 97%, **Scheme S6**).

3. Results and discussion

3.1. Materials characterization and structural investigation

We successfully synthesized three CMPs, namely AQ-HATN, PQ-HATN, and DPED-HATN CMPs via the Suzuki coupling method and using HATN as an electron-donating moiety and AQ-2Br, PQ-2Br, and DPED-2Br as the electron-withdrawing moieties, using PDBA as a linker and $Pd(PPh_3)_4$ as a catalyst to provide excellent features for the energy storage application, as illustrated in Schemes 1**(a.c)**. The chemical structures of the monomers were confirmed by FT-IR, NMR, and HR-ESI-MS analyses. For HATN-3Br, the FT-IR spectrum (**Fig. S1**) shows an aromatic C—H stretching band at 3067 cm^{-1} and a characteristic C=N stretching vibration at 1605 cm^{-1}. High-resolution mass spectrometry (**Fig. S2**) displays a molecular ion peak at $m/z = 621.84$, consistent with the calculated molecular weight. For AQ-2Br, the FT-IR spectrum (**Fig. S3**) exhibits aromatic C—H stretching at 3101 cm^{-1}, a strong C=O stretching band at 1677 cm^{-1}, and aromatic C=C stretching at 1583 cm^{-1}, characteristic of the anthraquinone structure. The ^{1}H NMR spectrum (**Fig. S4**) shows aromatic proton signals at $\delta = 8.66$, 7.92, and 7.76 ppm, while the ^{13}C NMR spectrum displays a characteristic carbonyl carbon resonance at $\delta = 179.66$ ppm (**Fig. S5**). Similarly, PQ-2Br presents FT-IR absorption bands at 3101 cm^{-1} (aromatic C—H), 1677 cm^{-1} (C=O), and 1583 cm^{-1} (aromatic C=C) (**Fig. S6**), and its ^{1}H NMR spectrum (**Fig. S7**) shows aromatic proton resonances at $\delta = 8.66$,

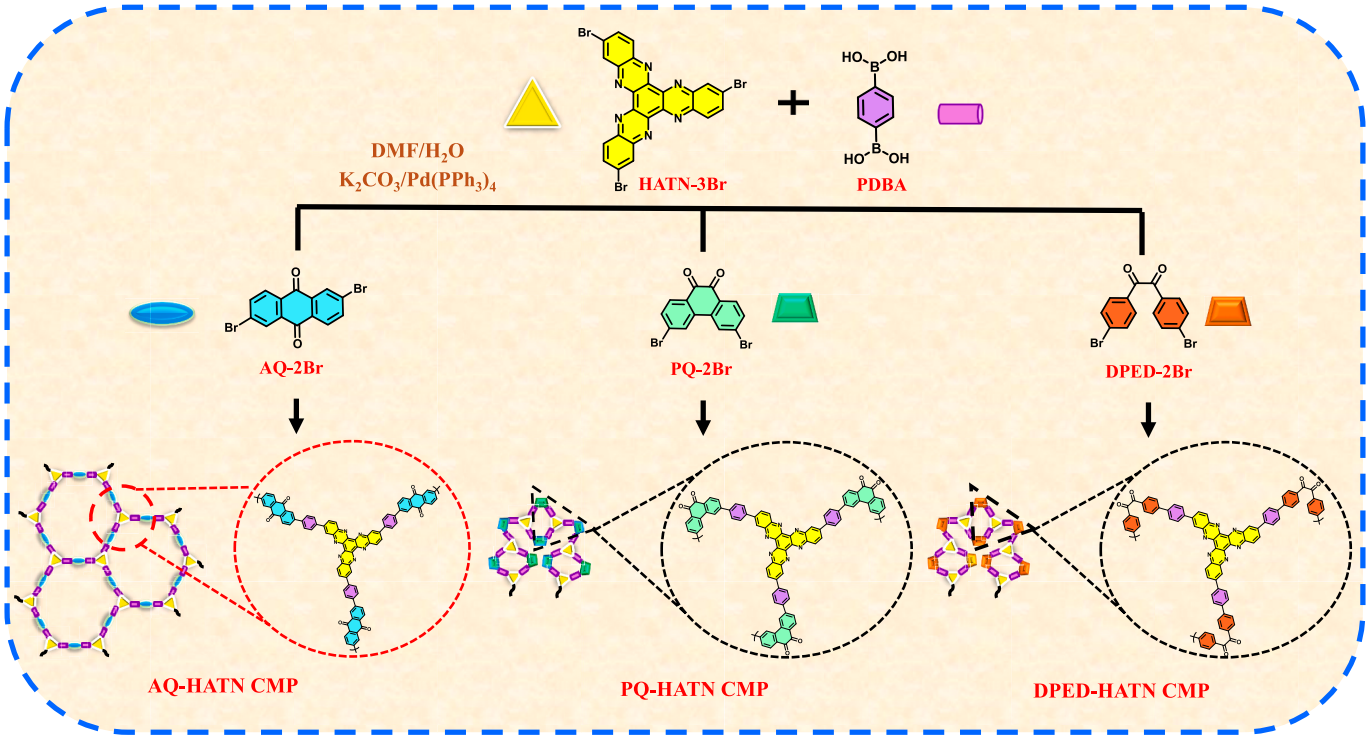

Scheme 1. Synthesis of AQ-HATN, PQ-HATN, and DPED-HATN CMPs.

7.92, and 7.76 ppm, confirming its molecular structure. We utilize various techniques to identify and characterize all monomers and CMPs. Firstly, we used Fourier transform infrared (FT-IR) to measure the different functional groups and bond vibrations in these CMPs, as illustrated in Fig. 1(a). The FT-IR spectra of AQ-HATN, PQ-HATN, and DPED-HATN CMPs demonstrated distinctive peaks for C—H aromatic, C═O, C═N, and C═C stretching vibrations. The small vibration bands at 3067, 3064, and 3050 cm^{-1} arise from the C—H aromatic bond [7]. The vibration appeared at 1670, 1643, and 1663 cm^{-1} for C═O in those CMPs. Also, the bands at 1584, 1595, and 1588 cm^{-1} for C═N and 1479, 1484, 1486 cm^{-1} for C═C in AQ-HATN, PQ-HATN, and DPED-HATN CMPs, respectively [5–7,34].

There is a small shift in the wavenumbers of CMPs relative to the initial monomers, indicating the polymeric backbone is fully formed. The chemical composition and structural identification can be investigated by solid-state ^{13}C NMR spectra. As illustrated in Fig. 1(b), three feature resonance peaks were observed in the spectra of AQ-HATN, PQ-HATN, and DPED-HATN CMPs, respectively. The peaks located at 178.02, 181.4, and 181.6 ppm corresponding to C═O in AQ-HATN, PQ-HATN, and DPED-HATN CMPs, respectively [29,34]. Whereas the peaks in the range of 118.52–150 ppm, attributed to aromatic carbon atoms, overlapped with C═N [54,55]. In addition, utilizing thermogravimetric analysis (TGA) in N_2 atmosphere at a rate of heating of 20 °C min^{-1} from 40 to 800 °C, the thermal behavior of the AQ-HATN, PQ-HATN, and DPED-HATN CMPs was investigated and portrayed in Fig. 1(c). It revealed that, all three CMPs had exceptional thermal stabilities, which were attributed to the strong bond formation between AQ, PQ, or DPED and HATN monomers by the Suzuki coupling reaction, which created a stiff aromatic framework. Additionally, compared to the PQ-HATN CMP (thermally stable up to 200 °C, T_{d10} = 412.37 °C, and char yield = 71.01%) and the DPED-HATN CMP (thermally stable up to 280 °C, T_{d10} = 526.37 °C, and char yield = 71.3%), the AQ-HATN CMP showed a greater char yield (char yield reached 75.8% and thermally stable up to 220 °C, T_{d10} = 479.9 °C). The X-ray powder diffraction (XRD) of AQ-HATN, PQ-HATN, and DPED-HATN CMPs showed no distinct diffraction peaks only two broad peaks due to the amorphous carbon at 2θ of 10° or 13.7° and 25.3° [56–59], which are anticipated for organic microporous polymers synthesized under nonreversible circumstances [60,61], and illustrated the amorphous nature of the synthesized polymers as shown in **Fig. S8**. Moreover, X-ray photoelectron spectroscopy (XPS) was conducted to determine the elemental distribution and chemical environments of AQ-HATN, PQ-HATN, and DPED-HATN CMPs [Fig. 1(d) and Fig. 2]. The XPS survey profile (Fig. 1(d)) confirms the emergence of characteristic signals corresponding to C, N, and O atoms in all CMPs [5–7]. The high-resolution C 1 s spectra of AQ-HATN, PQ-HATN, and DPED-HATN CMPs (Fig. 2**(a–c)** and **Table S1–S3**) each display a main peak deconvoluted into three components attributed to C–C/C=C, C–N/C=N, and C═O bonds. The C–C/C=C contributions are observed at 283.4, 283.42, and 283.34 eV for AQ-HATN, PQ-HATN, and DPED-HATN CMPs, respectively [62,63]. Peaks corresponding to C–N/C=N appear at 284.62, 284.43, and 284.72 eV, while those assigned to C═O are detected at 285.8, 284.9, and 285.4 eV, respectively [64,65]. The N 1 s spectra of AQ-HATN, PQ-HATN, and DPED-HATN CMPs (Fig. 2 **(d–f) and Table S1–S3**) can each be deconvoluted into two components associated with N═C and N—C bonds. The N═C signals appear at 397.61, 397.50, and 397.69 eV, whereas the N—C peaks are located at 398.24, 397.94, and 398.92 eV, respectively [7,66,67]. Furthermore, the O 1 s spectra (Fig. 2**(g–i) and Table S1–S3**) exhibit single dominant peaks corresponding to the C═O group, appearing at binding energies of 530.5, 531.0, and 531.05 eV, respectively [16,68]. The slight shifts in

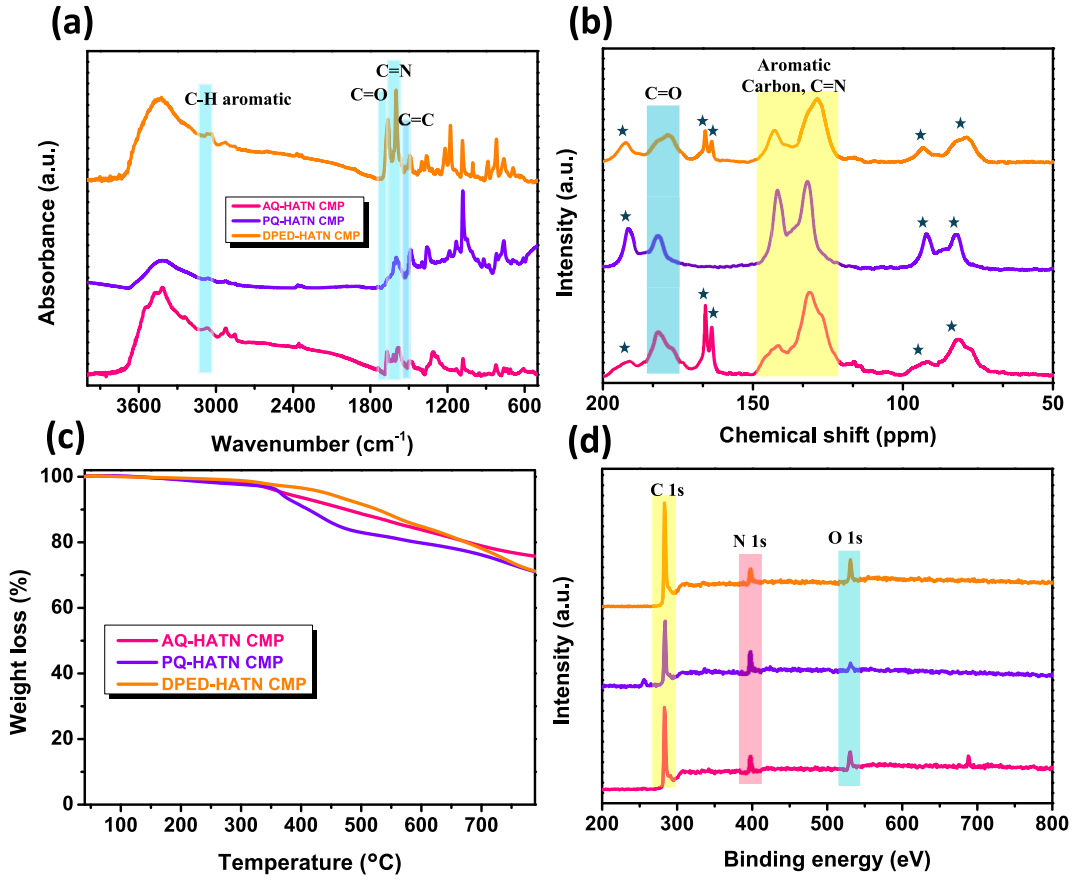

Fig. 1. Characterization of AQ-HATN, PQ-HATN, and DPED-HATN CMPs: (a) FTIR spectra, (b) solid-state ^{13}C NMR spectra, (c) TGA curves, and (d) XPS survey spectra.

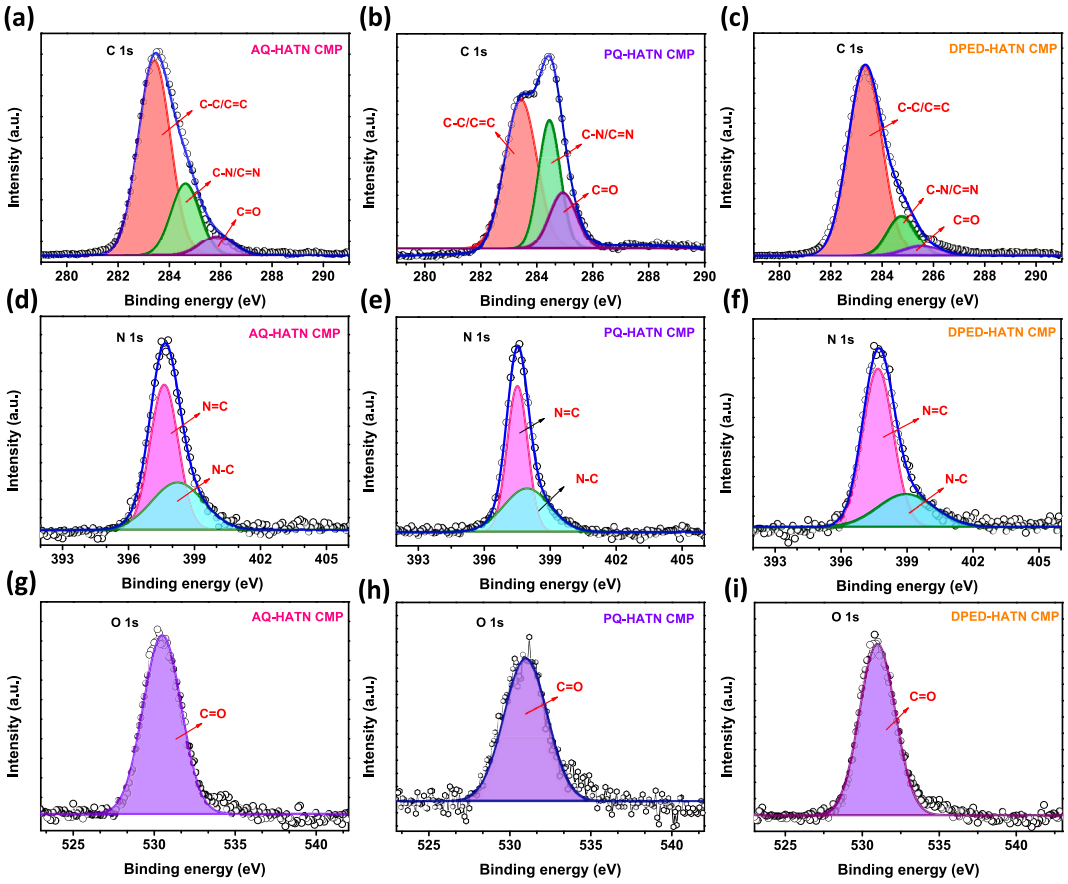

Fig. 2. High-resolution XPS spectra of AQ-HATN, PQ-HATN, and DPED-HATN CMPs: (a-c) C 1 s, (d-f) N 1 s, and (g-i) O 1 s regions of (a, d, g) AQ-HATN CMP, (b, e, h) PQ-HATN CMP, and (c, f, i) DPED-HATN CMP, respectively.

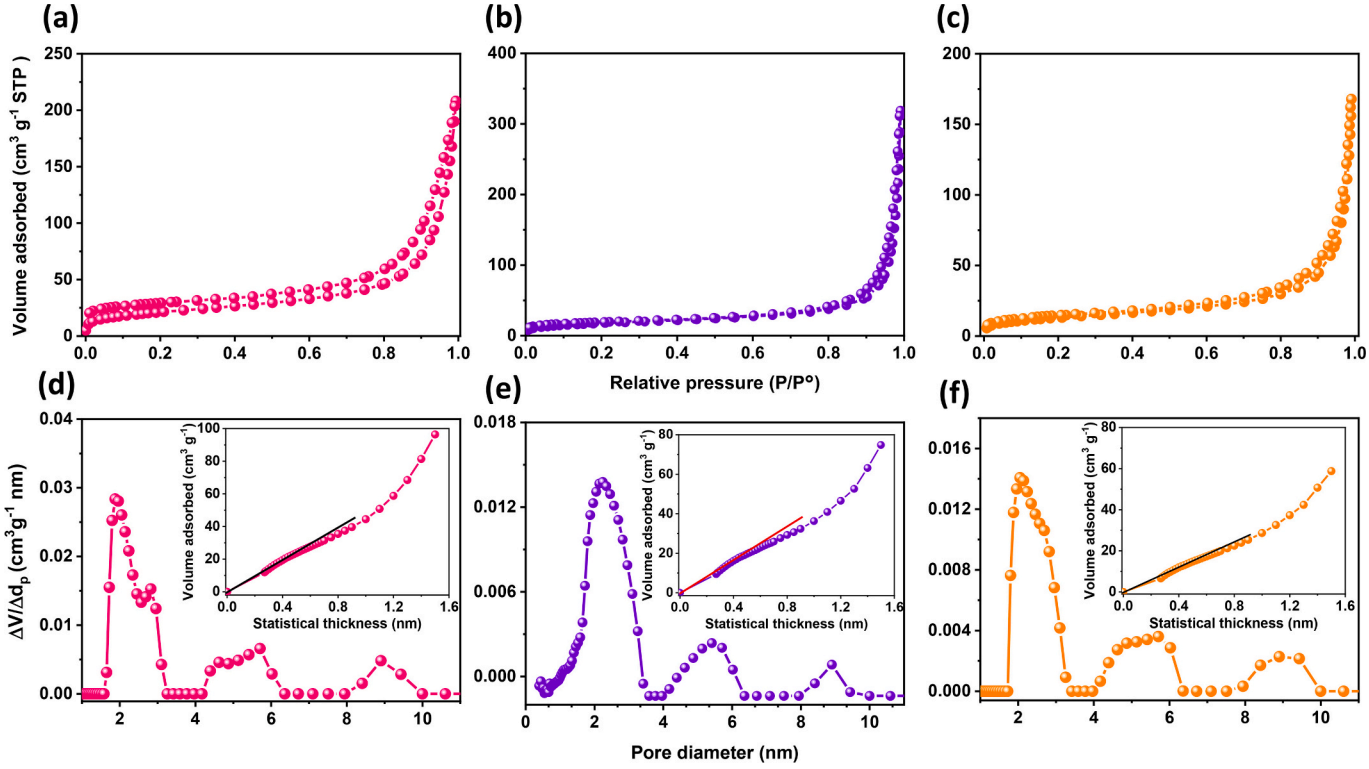

Fig. 3. N_2 adsorption-desorption isotherms (a–c) and pore size distribution curves (d–f) of (a, d) AQ-HATN CMP, (b, e) PQ-HATN CMP, and (c, f) DPED-HATN CMP. Insets in (d–f) display the corresponding *t*-plot (V_a-*t*) analyses.

the C═O and N-related binding energies among the three CMPs reflect variations in local electronic environments and charge delocalization around the carbonyl and imine functionalities, consistent with the distinct conjugation and steric effects imparted by the AQ, PQ, and DPED moieties within their CMP frameworks.

To investigate the porous architecture of the HATN-based CMPs, nitrogen adsorption–desorption isotherms were measured at −196 °C, with the results shown in Fig. 3. The isotherms (Fig. 3**(a–c)**) are primarily Type II with minor Type IV characteristics according to Brunauer's classification, indicating a hierarchical micro–mesoporous structure [6,7,21,33,69]. The H3-type hysteresis loops, with minor H2 contributions, suggest the predominance of wedge-shaped pores with some slit-like geometry [5,35,70]. The specific surface areas (S_{BET}), calculated over P/P_0 = 0.05–0.30, follow the trend AQ-HATN CMP (75.15 $m^2\ g^{-1}$) > PQ-HATN CMP (62.09 $m^2\ g^{-1}$) > DPED-HATN CMP (46.62 $m^2\ g^{-1}$), along with their respective total pore volumes of 0.32, 0.28, and 0.24 $cm^3\ g^{-1}$, respectively (**Table S4**). Consistent values obtained using the *t*-method (de-Bore approach) confirm the reliability of the measurements [71]. Pore size distributions derived from non-local density functional theory (NLDFT) (Fig. 3**(d–f)**) further verify hierarchical porosity. AQ-HATN CMP exhibits an optimal pore width range of 1.6–3.18 nm with an average diameter of 1.87 nm. In contrast, PQ-HATN and DPED-HATN CMPs display broader distributions of 0.4–3.55 nm and 1.71–3.66 nm, with average diameters of 2.18 and 2.30 nm, respectively. These broader pores can be attributed to the steric hindrance from the *peri-* and *vicinal* carbonyl arrangements in PQ and DPED, respectively, which distort molecular planarity and disrupt dense framework packing–generating mesoporous voids alongside constricted micropores in localized regions [41,72–79]. $V_a - t$ plots (**insets of Fig. 3 (d–f)**) further confirm the coexistence of micro and mesopores through characteristic downward–upward deviations [71]. Compared with PQ-HATN CMP and DPED-HATN CMP, the well-balanced pore hierarchy

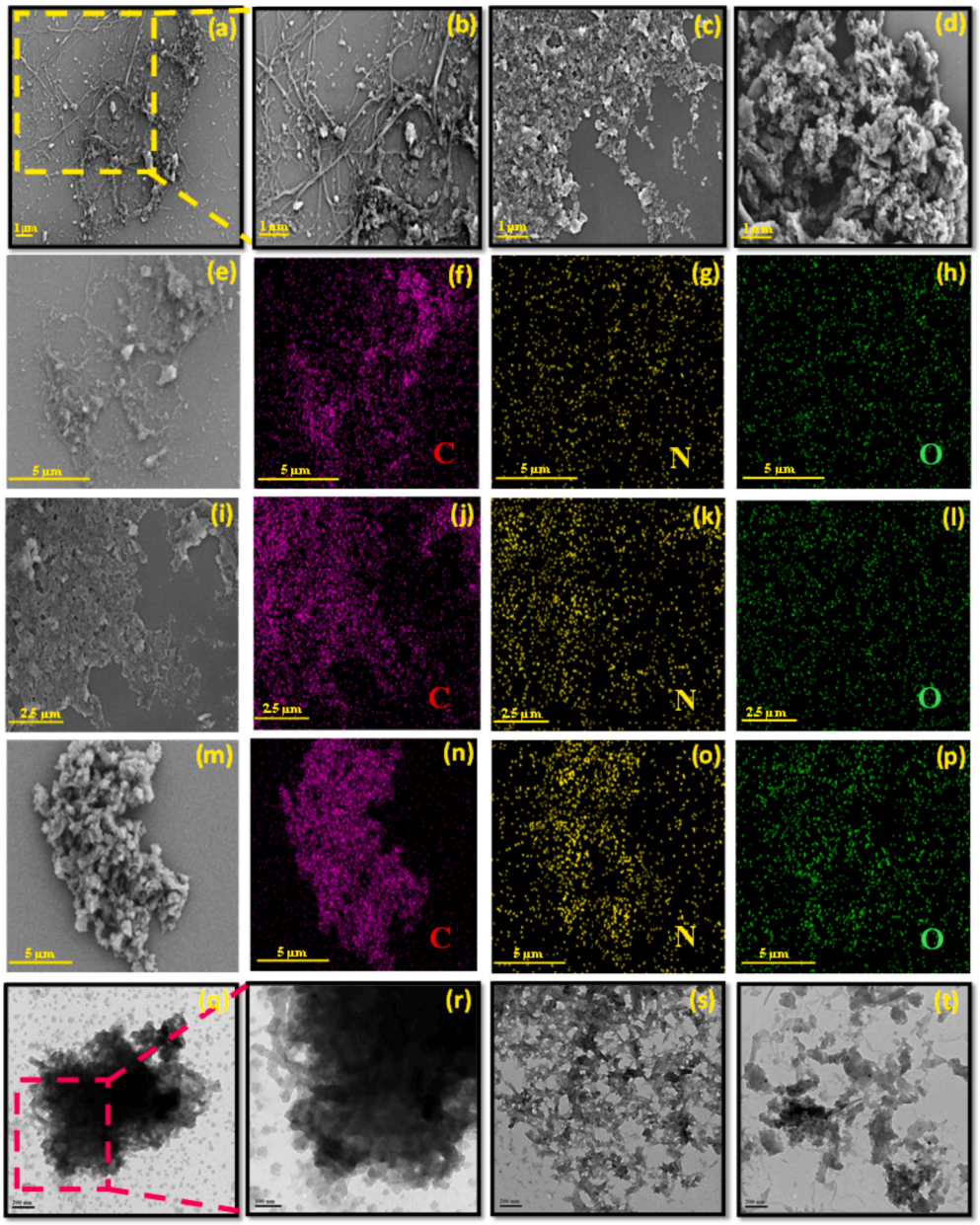

Fig. 4. (a–d) SEM images of (a, b) AQ-HATN CMP under different magnifications, (c) PQ-HATN CMP, and (d) DPED-HATN CMP. (e–p) EDS elemental mapping images of (e–h) AQ-HATN CMP, (i–l) PQ-HATN CMP, and (m–p) DPED-HATN CMP. (q–t) HR-TEM images of (q, r) AQ-HATN CMP under different magnifications, (s) for PQ-HATN, and (t) DPED-HATN CMP.

and relatively higher surface area of AQ-HATN CMP together provide an ideal environment that facilitates rapid ion diffusion and ensures full accessibility of redox-active sites. Conversely, PQ-HATN CMP possesses a fraction of sub-nanometer micropores that restrict electrolyte diffusion, while the larger and less densely distributed mesopores in DPED-HATN CMP decrease the density of accessible electroactive sites. These textural variations–rooted in the distinct carbonyl geometries and linker conformations of AQ, PQ, and DPED–ultimately govern ion-transport efficiency and charge-storage behavior within their CMP frameworks.

Scanning electron microscopy (SEM) images of AQ-HATN CMP (Fig. 4(a) and (b)) reveal interconnected rod-like structures forming a continuous network, which is more clearly observed at higher magnification (Fig. 4(b)). In contrast, SEM images of PQ-HATN and DPED-HATN CMPs (Fig. 4(c) and (d)) show aggregates that are irregularly shaped with numerous cavities. The corresponding energy-dispersive X-ray spectroscopy (EDS) elemental mapping (Fig. 4(e–p)) confirms the homogeneous distribution of C, N, and O across all samples. Transmission electron microscopy (TEM) and high-resolution TEM (HR-TEM) images of AQ-HATN CMP (Fig. 4(q) and (r)) further corroborate the SEM observations, showing nanorod- or nanosheet-like morphologies forming an open porous network that enhances ion accessibility.

The predominantly amorphous features observed in **Fig. S8** are consistent with the hierarchical micro–mesoporous structures revealed by BET analysis and the open, interconnected morphologies observed in SEM and TEM images, which collectively facilitate efficient ion diffusion and full accessibility of redox-active sites in the AQ-HATN CMP. In contrast, PQ-HATN and DPED-HATN CMPs (Fig. 4(s) and (t)) consist of nanoscale particles with irregular shapes, forming less ordered but still porous networks. The morphological irregularity of PQ-HATN and DPED-HATN CMPs arises from the steric effects introduced by the *peri*- and *vicinal*-carbonyl geometries, respectively. These morphology–structure correlations align well with the nitrogen sorption analyses, confirming that the planar *para*-carbonyl geometry in AQ-HATN CMP supports a more ordered framework and well-balanced pore hierarchy, while the sterically hindered linkers in PQ- and DPED-HATN CMPs yield broader pore distributions that limit ion accessibility and charge transport efficiency.

3.2. Electrochemical performance

3.2.1. Electrochemical performance of the AQ-HATN, PQ-HATN and DPED-HATN CMPs evaluated in a three-electrode configuration

To explore the electrochemical characteristics of the HATN-based CMPs—namely AQ-HATN, PQ-HATN, and DPED-HATN CMPs—as promising electrode materials for supercapacitors, cyclic voltammetry (C*V*) and galvanostatic charge–discharge (GCD) analyses were performed in a three-electrode configuration within an alkaline aqueous electrolyte (1 M KOH). The electrochemical tests were carried out over a potential range of −0.15 to −1.15 *V* vs. Hg/HgO, employing a glassy carbon electrode as the working electrode, Hg/HgO as the reference electrode, and a platinum (Pt) mesh as the counter electrode. Fig. 5**(a–d)** displays the CV curves of AQ-HATN, PQ-HATN, and DPED-HATN CMPs recorded at scan rates ranging from 5 to 100 m*V* s^{-1}. **Fig. S9** displays CV curves of AQ-HATN, PQ-HATN, and DPED-HATN CMPs recorded at scan rates of 1–10 mV s^{-1}. The CV curves of the three HATN-based CMPs are characterized by two distinct pairs of redox peaks, indicating multi-step redox reaction arising from their abundant redox-active centers and confirming their Faradaic charge-storage behavior [32,33,80,81]. The first redox couple appears around −0.564 to −0.662 *V* vs. Hg/HgO, corresponding to a reversible multi-electron redox reaction of the imine (C=N) functional groups in the HATN moiety; whereas the second redox couple appears at more negative potentials (−0.75 to −0.88 V), corresponding to a reversible redox reaction of the carbonyl (C=O) functional groups in the incorporated quinone (e.g., AQ, or PQ) or benzil (DPED) units [32–40,78,80,81]. At 5 mV s^{-1}, the first redox couple of AQ-HATN CMP (Fig. 5(a)) is observed with cathodic and anodic peaks at −0.662 and − 0.613 *V* vs. Hg/HgO, respectively. The second redox couple appears at a more negative potential, showing a broad cathodic peak centered at −0.878 *V* and an anodic peak at −0.783 V vs. Hg/HgO. In the CV curves (Fig. 5(a)), the dashed and solid lines represent the anodic and cathodic peaks, respectively, for the first and second redox couples of all three HATN-based CMPs. The first redox couple corresponds to a reversible one-step multi-electron redox reaction of the imine (C=N) functional groups in the HATN moiety [48–52]; whereas the second redox couple corresponds to a reversible one-step redox reaction of the C=O functional groups in the AQ moiety [45,81]. For PQ-HATN CMP (Fig. 5(a)), the first redox couple is observed with cathodic and anodic peaks at −0.634 and − 0. 594 *V* vs. Hg/HgO, respectively. The second

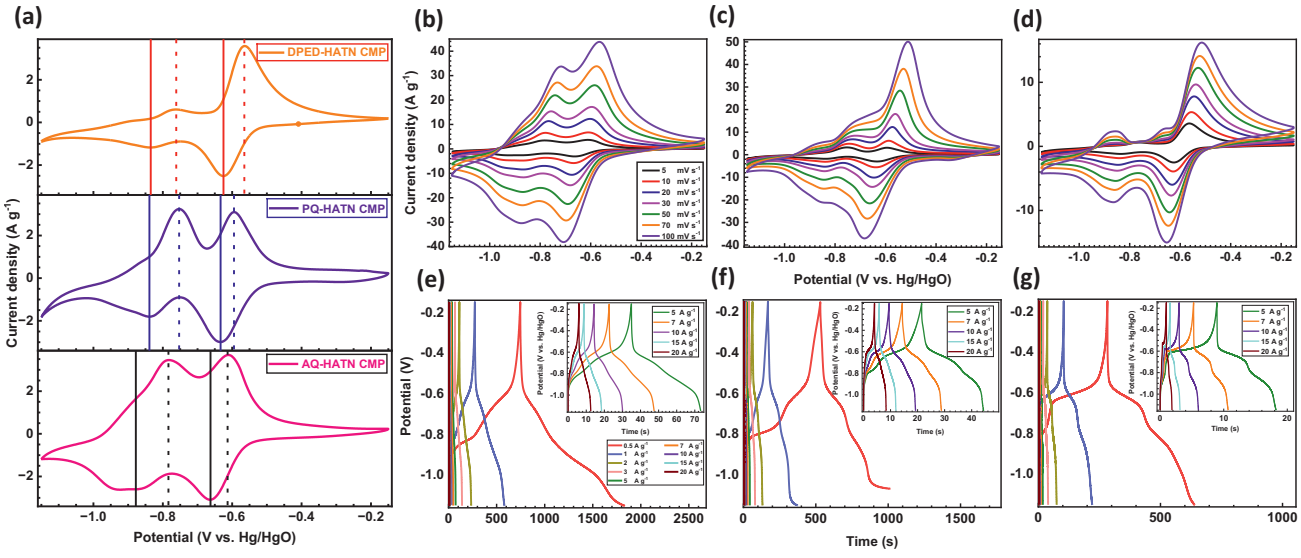

Fig. 5. (a) CV curves of AQ-HATN, PQ-HATN, and DPED-HATN CMP electrodes at a scan rate of 5 mV s^{-1}, (b–d) CV curves of (b) AQ-HATN CMP, (c) PQ-HATN CMP, and (d) DPED-HATN CMP recorded at scan rates ranging from 5 to 100 mV s^{-1}, (e–g) GCD curves of (e) AQ-HATN CMP, (f) PQ-HATN CMP, and (g) DPED-HATN CMP recorded at current densities ranging from 0.5 to 20 A g^{-1}. Insets of (e–g) display magnified GCD curves at higher current densities.

redox couple features a broad cathodic peak centered at −0.839 V and an anodic peak at −0.753 V vs. Hg/HgO, which corresponds to a reversible one-step redox reaction of the carbonyl (C=O) functional groups in PQ moiety [36,81]. Notably, the HATN-related redox peaks of PQ-HATN CMP are slightly shifted to more positive potentials compared to AQ-HATN CMP (Fig. 5(a)), suggesting that the electronic environment of the HATN core is influenced by the positional nature of the carbonyl-groups within the appended quinone moieties [41,81]. Similarly, the CV curve of DPED-HATN CMP (Fig. 5(a)) shows its first redox couple with cathodic and anodic peaks at −0.625 and − 0.564 V vs. Hg/HgO, respectively. The second redox couple appears with broad cathodic and anodic peaks centered at −0.835 and − 0.762 V vs. Hg/HgO, respectively, attributable to a reversible one-step redox reaction of the carbonyl (C=O) functional groups in DPED [78]. The HATN-related redox peaks of DPED-HATN CMP are further shifted to more positive potentials compared to both AQ-HATN CMP and PQ-HATN CMP (Fig. 5 (a)), reflecting how the electronic environment of the HATN core is modulated by the positional nature of the carbonyl-groups within the appended quinone (e.g., AQ, and PQ) and benzil (DPED) moieties. AQ, featuring a *para*-diketone configuration at the 9,10-positions, adopts a highly planar geometry that facilitates extended π-conjugation across the aromatic framework [82,83]. In contrast, PQ contains carbonyl groups at the 9,10-positions of the phenanthrene framework, adjacent in bonding but conventionally described as *peri*-positions in fused aromatic systems [72–74]. The close spatial proximity of these *peri*-carbonyls induces steric and electronic repulsion (the *peri*-effect), which distorts planarity, disrupts π-conjugation, and shifts the redox potential positively [41,72–74,79]. DPED, bearing a *vicinal* 1,2-diketone separated by a single σ-bond, restricts electronic communication between the two carbonyl redox centers [75–77]. This configuration, coupled with strong electron-withdrawing character and pronounced steric hindrance, results in the most positive redox potentials among the three HATN-based CMPs [75–78]. These findings demonstrate that subtle variations in carbonyl positioning offer a rational molecular strategy for tuning the redox properties of HATN-based CMPs. Peak separation (ΔE_p), between the anodic and cathodic waves, provides further insight into the redox kinetics of the HATN-based CMPs. For AQ-HATN CMP, the first and second redox couples exhibit ΔE_p values of ~49 and 95 mV, respectively, (**Table S5–S7**). In PQ-HATN CMP, ΔE_p values of ~40 and 86 mV are obtained, while DPED-HATN CMP shows ΔE_p values of ~61 and 73 mV for the first and second redox couples, respectively. These relatively small ΔE_p values indicate that the redox processes in all three HATN-based CMPs are reasonably reversible [38], suggesting fast electron-transfer kinetics and efficient ion transport within their porous frameworks, which are favorable characteristics for high-performance supercapacitor electrodes. Upon increasing the scan rate within the range of 5–100 mV s^{-1}, a simultaneous enhancement in both cathodic and anodic peak current densities increased proportionally while the overall shape of the CV curves was retained, as demonstrated in Fig. 5**(b–d)**. However, the corresponding redox peak potentials shifted toward more negative values for the cathodic peaks and more positive values for the anodic peaks, leading to a progressive widening of ΔE_p with increasing scan rate (**Table S5–S7**). These features reveal that the redox processes are quasi-reversible in nature, being influenced by both electron-transfer kinetics and ion-diffusion constraints within the CMP frameworks [38,41]. Interestingly, upon increasing the scan rate to 100 mV s^{-1}, the carbonyl (C=O) oxidation process gradually evolved into two broad peaks for both PQ-HATN and DPED-HATN CMPs (Fig. 5(c) and (d)). This behavior suggests that the two C=O groups in these CMPs, which undergo nearly simultaneous redox at slow scan rates, become kinetically distinguishable at higher scan rates as a result of increasing polarization and ion-diffusion limitations within the CMP framework. The splitting of the oxidation peak thus reflects the stepwise electron-transfer processes of the two carbonyl centers, which remain overlapped under near-equilibrium conditions but become resolved when the system is subjected to faster potential sweeps [84,85]. Fig. 5**(e–g)** shows the GCD profiles of AQ-HATN, PQ-HATN, and DPED-HATN CMPs, recorded across a range of current densities from 0.5 to 20 A g^{-1}. In the GCD profiles of the three HATN-based CMPs, the coexistence of HATN and quinone (e.g., AQ, or PQ) or benzil (DPED) redox moieties is evidenced by distinct voltage plateaus superimposed on the quasi-triangular charge-discharge curves. The nearly linear regions can be ascribed to the electric double-layer capacitance (EDLC) contribution of the porous conjugated framework, whereas the plateaus arise from Faradaic redox processes. As shown in Fig. 5**(e–g)**, two plateaus are observed. The first plateau, appearing at higher potentials (around −0.6 *V* vs. Hg/HgO), is assigned to the reversible multi-electron redox reactions of the imine (C=N) groups in the HATN moiety. At more negative potentials (around −0.90 to −1.0 V vs. Hg/HgO), a second plateau emerges, corresponding to the reversible redox reactions of the carbonyl (C=O) groups in the quinone (e.g., AQ, or PQ) or benzil (DPED) moieties. The coexistence of these two redox systems within the same framework enables multiple electron-transfer processes over a wide potential window, thereby enhancing the charge-storage capacitance. Furthermore, the relatively symmetric charge–discharge curves suggest good reversibility of these redox reactions and stable cycling behavior, which are highly desirable for supercapacitor electrode applications.

Fig. 6(a) depicts the electrochemical capacitance values of the three HATN-derived CMP electrodes, determined from the GCD data at various current densities according to **Eq. S1**. The maximum capacitances were observed at 0.5 A g^{-1} with values of 543.4 ± 4.2, 230.5 ± 3.7, and 178.45 ± 3.9 F g^{-1} for AQ-HATN, PQ-HATN, and DPED-HATN CMPs, respectively. As the current density increased from 0.5 to 20 A g^{-1}, the specific capacitance values of the three HATN-based CMPs continuously decreased. This behavior is commonly observed in porous redox-active electrode materials and can be ascribed to kinetic and mass transport limitations [7]. At lower current densities, electrolyte ions have sufficient time to penetrate the internal pores of the CMP frameworks, enabling full utilization of both the C=O and imine (C=N) redox-active sites. However, as the current density increases, the charge–discharge process becomes much faster, restricting ion diffusion to only the more accessible surface and near-surface sites. Consequently, a portion of the redox-active sites embedded deeper within the porous framework remains unutilized, leading to a reduction in the measured capacitance. The Ragone plots (Fig. 6(b)) show that the AQ-HATN CMP delivered the highest energy density value of 75.47 ± 0.6 Wh Kg^{-1} at a power density of 250 W Kg^{-1} in the three electrode configuration. These values markedly outperform the reported state-of-the-art quinone-based electrodes, as demonstrated in Fig. 6(c) and **Table S8**. Representative examples include: *ortho*-quinone-embedded COF (INIT-1, 6.66 F g^{-1} at 0.5 A g^{-1}) [10], phenanthrenequinone (PQ, 66 F g^{-1} at 2 A g^{-1}) [11], Onion like carbons (OLC) functionalized with 4,5-pyrenedione (PY-OLC), 1,4-naphthoquinone (NQ-OLC), and PQ (PQ-OLC), which deliver 130, 91, and 267 F g^{-1}, respectively, at 5 mV s^{-1} [32]. Other reported systems include 9,10-phenanthrenequinone-based 2D COFs (2KT-Tp and 4KT-Tp COFs, 155 and 340 F g^{-1} at 0.5 A g^{-1}) [33], TPA-PT and BC-PT CMP (204 and 373 F g^{-1} at 1 A g^{-1}) [34], hierarchical porous rGO/9,10-phenanthraquinone (RP, 277.7 F g^{-1} at 0.5 A g^{-1}) [35], non-covalently modified rGO/PQ (RGO/PQ-1.5, 383.3 F g^{-1} at 0.5 A g^{-1}) [36], An-TPT POP (39.63 F g^{-1} at 1 A g^{-1}) [29], pure Anthraquinone (Pure AQ) (42 F g^{-1} at 1 A g^{-1}) [37], *β*-ketoenamine-linked DAAQ-TFP COF (48 F g^{-1} at 0.1 A g^{-1}) [38], Anthraquinone-based HcDa COF (71.25 F g^{-1} at 1 A g^{-1}) [39], BF-DTDO CMP (95.62 F g^{-1} at 0.5 A g^{-1}) [5], Anthraquinone/MXene CMPs (PAQBz and M-PAQBz, 106 and 190 F g^{-1} at 0.3 A g^{-1}) [43], and triphenylpyridine-linked dithiophene-4,8-dione CMPs (TPP-DBTh and BTPP-DBTh CMPs, 221.86 and 143.27 F g^{-1} at 0.5 A g^{-1}) [42]. In addition, hybrid and molecular systems such as ultrasonic hybrid Rhein/porous lignin-based graphitic carbon (RH/PLGC = 1, 250.2 F g^{-1} at 1 A g^{-1}) [45], donor–acceptor (D–A) system based on 3,6-di-tert-butyl-9H-carbazole and fused pyrazine-anthraquinone (DTCz-Pyz-AQ/GF, 304.37 F g^{-1} at 0.5 A g^{-1}) [46],

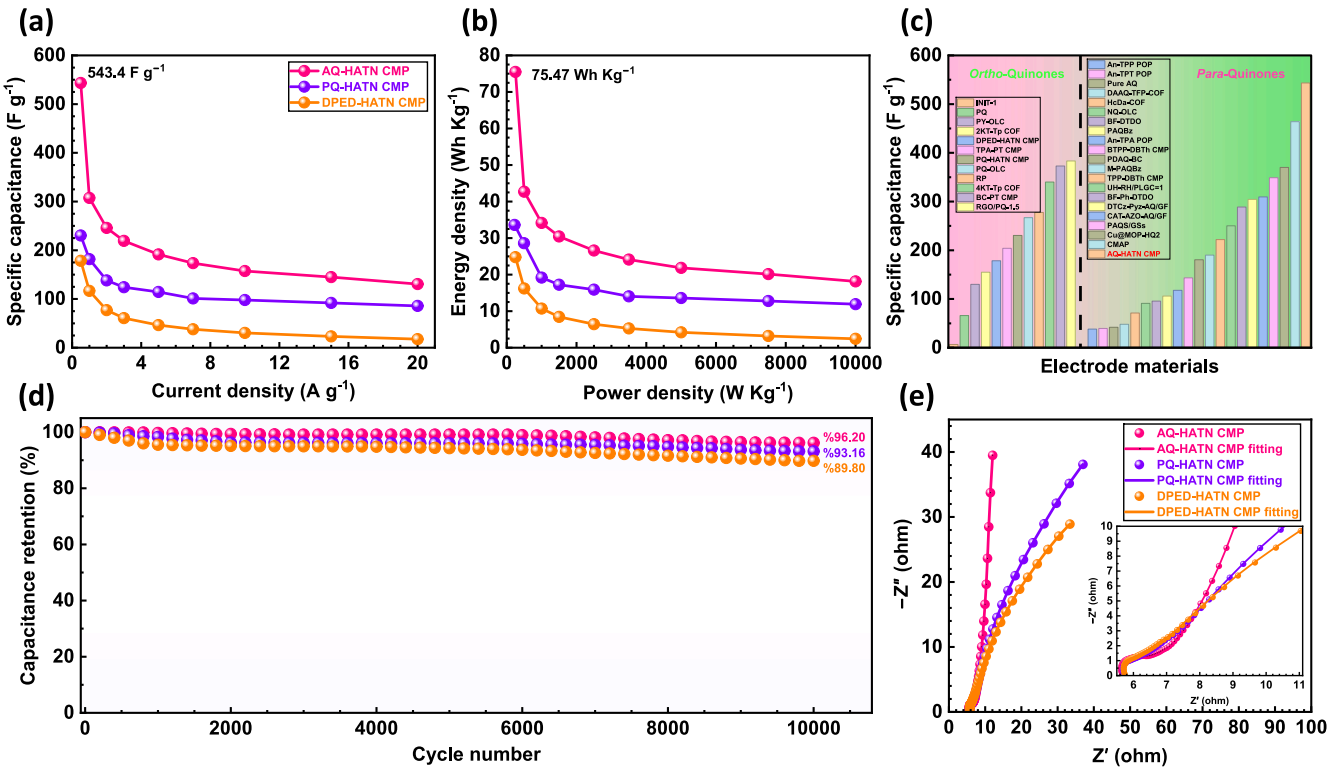

Fig. 6. (a) Specific capacitance values calculated from GCD curves at current densities of 0.5–20 A g^{-1}, (b) Ragone plots, (c) Comparative analysis with previously reported redox-active polymers, (d) Cycling stabilities at a current density of 10 A g^{-1}, and (e) Nyquist plots and their fitted plots of AQ-HATN, PQ-HATN, and DPED-HATN CMPs. The inset of (e) displays the high-frequency region.

and CAT-AZO-AQ/GF (309.58 F g^{-1} at 0.5 A g^{-1}) [47] have also been reported. Cycle stability serves as an important criterion for evaluating the suitability of electrode materials for practical supercapacitor applications. Fig. 6(d) shows the cyclic performance of the three HATN-based CMPs electrodes over 10,000 cycles at 10 A g^{-1}. The AQ-HATN, PQ-HATN, and DPED-HATN CMP electrodes exhibit excellent stability, retaining 96.20%, 93.16%, and 89.8% of their initial capacitance, respectively. Electrochemical impedance spectroscopy (EIS) was performed to investigate the charge-transfer kinetics and resistance characteristics of the HATN-based CMPs electrodes. The measurements were conducted at open-circuit potential with 5 mV amplitude. Fig. 6(e) and **Fig. S10** present the Nyquist plots and the corresponding equivalent circuit model fitted to the experimental data for AQ-HATN, PQ-HATN, and DPED-HATN CMP electrodes. In the Nyquist plots, the intercept with the real axis (X-axis) corresponds to the equivalent series resistance (R_s), which includes the combined resistance of the electrode material, electrolyte, current collector, and interfacial contacts. The calculated R_s values for AQ-HATN, PQ-HATN, and DPED-HATN CMP electrodes were 5.704, 5.758, and 5.782 Ω, respectively (**Table S9**). The plots feature small semicircles in the high-frequency region, corresponding to the charge-transfer resistance (R_{ct}) at the electrode/electrolyte interface, followed by nearly vertical lines in the low-frequency region, representing Warburg impedance (W_o) associated with ion diffusion within the porous network. A steeper slope in the low-frequency region indicates faster ion diffusion, reflection more efficient ion transport, and superior capacitive behavior [34–36]. The obtained fitting results reveal that AQ- HATN CMP possesses the lowest R_s (5.704 Ω) and R_{ct} (1.5 Ω) (**Table S9**), highlighting its superior electrochemical behavior arising from enhanced conductivity and efficient charge transfer. In contrast, DPED-HATN CMP shows the highest R_s (5.782 Ω) and R_{ct} (12.48 Ω), reflecting greater resistance and inferior charge storage capability. Moreover, the steeper Warburg slope in the low-frequency region for AQ-HATN CMP compared to PQ- and DPED-HATN CMPs indicates enhanced ion diffusion, which can be attributed to the favorable positioning of carbonyl groups in AQ relative to PQ and benzil. These findings underscore AQ-HATN CMP as the most promising candidate, owing to its minimal resistance and excellent charge transfer characteristics, and further imply that the carbonyl group positioning plays a decisive role in governing ion transport dynamics in HATN-based CMPs.

The redox process of AQ-HATN CMP is illustrated in Fig. 7(a–c), which arises from the combined contributions of the AQ and HATN moieties. The HATN unit undergoes a multi-electron reduction to form the $HATN^{6-}$ anion (Fig. 7(a)) [7,80], while the AQ unit undergoes a two-electron reduction to yield the AQ^{2-} anion (Fig. 7(b)) [13,14]. These complementary redox activities endow the AQ-HATN CMP with a pronounced pseudocapacitive character. As depicted in Fig. 7(c), both the AQ and HATN components are reduced during the discharge process, whereas oxidation of the corresponding AQ^{2-} and $HATN^{6-}$ species occurs during charging. The individual redox reactions of the AQ and HATN units are evidenced by the appearance of two distinct pairs of redox peaks at −0.878/−0.783 *V* and − 0.662/−0.613 V vs. Hg/HgO, respectively, in the CV curve (Fig. 5(a)). The coexistence of these redox couples confirms the dual redox contribution and the synergistic charge-storage behavior of the AQ-HATN CMP. The redox process of AQ-HATN CMP is illustrated in Fig. 7(a–c), which arises from the combined contributions of the AQ and HATN moieties. The HATN unit undergoes a multi-electron reduction to form the $HATN^{6-}$ anion (Fig. 7(a)) [7,80], while the AQ unit undergoes a two-electron reduction to yield the AQ^{2-} anion (Fig. 7(b)) [13,14]. These complementary redox activities endow the AQ-HATN CMP with a pronounced pseudocapacitive character. As depicted in Fig. 7(c), both the AQ and HATN components are reduced during the discharge process, whereas oxidation of the corresponding AQ^{2-} and $HATN^{6-}$ species occurs during charging. The individual redox reactions of the AQ and HATN units are evidenced by the appearance of two distinct pairs of redox peaks at −0.878/−0.783 *V* and − 0.662/−0.613 V vs. Hg/HgO, respectively, in the CV curve (Fig. 5(a)). The

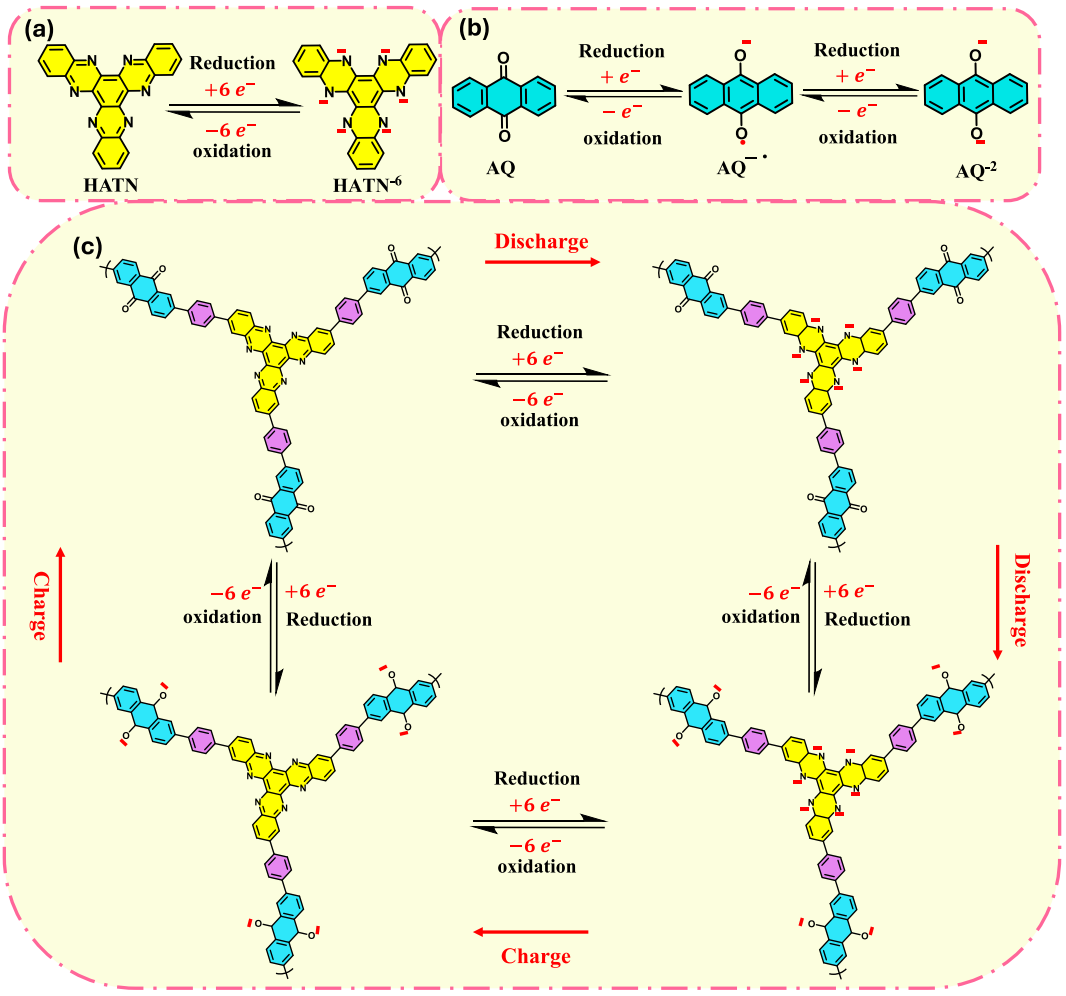

Fig. 7. (a–c) Suggested redox reactions of (a) HATN, (b) AQ, and (c) AQ-HATN CMP.

coexistence of these redox couples confirms the dual redox contribution and the synergistic charge-storage behavior of the AQ-HATN CMP. Similarly, **Fig. S11(a) and (b)** and **Fig. S12(a) and (b)** depict the redox process of PQ-HATN CMP and DPED-HATN CMP, respectively, which originates from the coupling of PQ or DPED linkers with the HATN core. In the CV curves (Fig. 5(a)), two pairs of redox peaks at −0.839/−0.753 V and − 0.634/−0.594 V vs. Hg/HgO for PQ-HATN CMP, assigned to redox reaction of PQ ⇌ PQ^{2-} and HATN ⇌ $HATN^{6-}$ moieties, respectively. Likewise, two pairs of peaks at −0.835/−0.762 V, and − 0.625/−0.564 V vs. Hg/HgO observed for DPED-HATN, corresponding to redox reactions of DPED ⇌ $DPED^{2-}$, and HATN ⇌ $HATN^{6-}$ moieties, respectively. These results collectively confirm that all three CMPs exhibit dual and reversible faradaic processes involving both the carbonyl linkers and HATN units, consistent with their pseudocapacitive charge-storage mechanism.

To further examine the capacitive characteristics of the HATN-based CMPs, the correlation between current *(i)* and scan rate *(ν)* is described by the power-law equation (Eq. (1)) [47,48] was employed to elucidate the charge-storage mechanism and quantify the capacitive contributions of AQ-HATN, PQ-HATN, and DPED-HATN CMPs:

$$i = av^b \tag{1}$$

where *a* and *b* are adjustable constants, and *b* is determined from the slope of the log*(i)*-log*(ν)* plot. When *b* equals 1, the charge storage is primarily governed by a capacitive-controlled mechanism, while a value near 0.5 denotes a diffusion-controlled mechanism. As presented in Fig. 8(a-c), the calculated *b* values for AQ-HATN CMP were 0.862 and 0.846 for the cathodic and anodic peaks, respectively (Fig. 8(a)), while PQ-HATN CMP attained values of 0.857 (cathodic) and 0.954 (anodic) (Fig. 8(b)). In contrast, DPED-HATN CMP exhibited considerably lower *b* values of 0.617 (cathodic) and 0.540 (anodic) (Fig. 8(c)). The results imply that the charge-storage behavior of all three CMPs arises from a combination of capacitive- and diffusion-controlled mechanisms, with AQ-HATN CMP showing the highest capacitive-controlled contribution. The quantitative capacitive and diffusion-controlled contributions were further evaluated using the Dunn method [5–7], expressed as:

$$i(V) = k_1 v + k_2 v^{1/2} \tag{2}$$

where $k_1 v$ represents the capacitive current, $k_2 v^{1/2}$ represents the diffusion-controlled current, and *i(V)* is the total current at a given potential *V*. As presented in Fig. 8(d–f), the capacitive contributions at 10 mV s^{-1} were determined to be 57% for the AQ-HATN CMP, 52% for the PQ-HATN CMP, and 26% for the DPED-HATN CMP. Fig. 8(g–i) further illustrates the variation in capacitive anddiffusion-controlled contributions over scan rates ranging from 1 to 100 mV s^{-1}. As the scan rate increases, the diffusion-controlled contribution decreases due to the shorter ion diffusion time within the CMP networks, while the surface-controlled process becomes increasingly dominant [64,65]. At 1 mV s^{-1}, the capacitive-controlled contributions were 30%, 25%, and 10% for AQ-HATN, PQ-HATN, and DPED-HATN CMPs, respectively, confirming the remarkable capacitive properties of the AQ-HATN CMP over those of both PQ-HATN and DPED-HATN CMPs. As the scan rate increased from 1 to 100 mV s^{-1}, the proportion of capacitive-controlled charge storage increased significantly, reaching 81% for the AQ-HATN

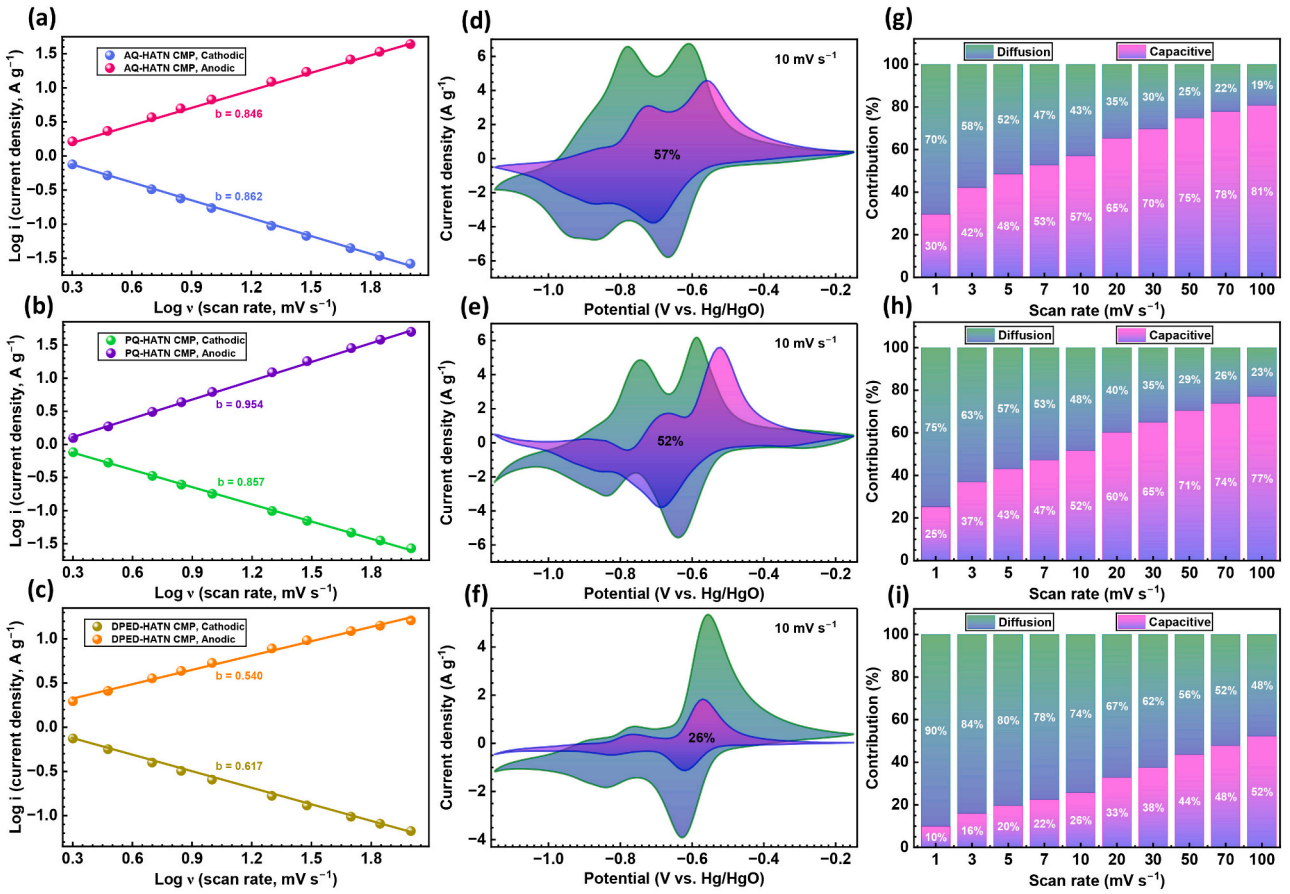

Fig. 8. log (*i*)-log (*v*) plots (a–c), separation of capacitive and diffusion-controlled contributions at a scan rate 10 mV s^{-1} (d–f), and variation of the two charge-storage components with scan rates (g–i) for (a, d, g) AQ-HATN CMP, (b, e, h) PQ-HATN CMP, and (c, f, i) DPED-HATN CMP.

(Fig. 8(g)), 77% for the PQ-HATN (Fig. 8(h)), and 52% for the DPED-HATN (Fig. 8(i)), thereby confirming the pseudocapacitive nature of these materials. In addition, AQ-HATN CMP exhibits the highest capacitive-controlled contribution among the studied samples, which can be attributed to the distinct structural characteristics of the incorporated carbonyl-containing units.

The AQ-HATN CMP, featuring a *para*-diketone linker, enforces molecular planarity and extended π-conjugation, while XPS confirms favorable electronic environments at the carbonyl and imine sites that facilitate efficient charge transfer. It's optimized micro–mesoporous network and interconnected rod-like morphology maximize redox-site accessibility and enable rapid ion diffusion. In contrast, PQ- and DPED-HATN CMPs, with *peri*- and *vicinal*-diketone linkers, exhibit distorted frameworks, disrupted conjugation, uneven charge distribution, and irregular porosity, which limit ion transport and reduce capacitance. These findings highlight that precise carbonyl positioning governs framework planarity, conjugation, porosity, and charge delocalization, collectively determining ion transport and redox accessibility, with AQ-HATN CMP achieving superior capacitive performance relative to its *peri*- and *vicinal*-diketone analogues. To verify the excellent cycling stability, after 10,000 successive charge–discharge cycles, the chemical stability of the HATN-based CMP electrodes was evaluated by comparing their XPS and FTIR spectra before and after cycling **(Fig. S13 and Fig. S14)**. The high-resolution C 1 s spectra demonstrate that the characteristic C═O signal associated with quinone-type carbonyl groups is clearly preserved after cycling, with no peak disappearance or formation of new carbon species. The dominant C–C/C=C and C–N/C=N contributions also remain essentially unchanged, with only minor binding-energy shifts attributable to the presence of Nafion binder and carbon black conductive additive [86]. These observations confirm that the π-conjugated CMP backbone remains structurally intact during prolonged electrochemical operation. Additional low-intensity C 1 s features at 288.1, 291.1, and 291.9 eV are assigned to C–SO_3, C—F, and CF_2 species originating from Nafion, rather than degradation of the CMP framework. Consistently, the N 1 s spectra exhibit negligible changes in the relative intensities of N═C and N—C components before and after cycling, confirming the high stability of the nitrogen-containing active sites. In the O 1 s region, a slight increase in oxygen-related components at approximately 533 and 535 e*V*, corresponding to C–O–C and O_3S–C species, is observed after cycling, which can be attributed to Nafion incorporation and interfacial interactions developed during electrochemical operation [87]. Importantly, the characteristic carbonyl-related C═O signals remain clearly discernible, providing direct chemical evidence for the excellent reversibility and stability of the redox-active carbonyl groups under long-term cycling conditions. These post-cycling XPS results unambiguously demonstrate that the carbonyl functionalities in all three HATN-based CMPs undergo highly reversible redox processes without irreversible conversion or degradation, thereby ruling out the possibility that the observed cycling stability arises from compensation by non-carbonyl sites. The robustness of the carbonyl groups is attributed to their incorporation within a rigid, π-conjugated CMP framework, which stabilizes the redox-active sites and suppresses dissolution or structural rearrangement during repeated cycling.

3.2.2. Electrochemical performance of the AQ-HATN, PQ-HATN and DPED-HATN CMPs evaluated in a two-electrode configuration

To assess the practical applicability of HATN-based CMPs as electrode materials in supercapacitors, symmetric devices (HATN-based CMP//HATN-based CMP) were assembled in a two-electrode setup using 3 M KOH electrolyte. C*V* measurements were conducted from 0.00

to 1.2 V at 5–100 mV s^{-1} using identical electrodes separated by a filter paper membrane. No significant polarization was observed within this voltage range; therefore, the operating voltage of the SSC devices was set at 0–1.2 V. Fig. 9**(a–c)** presents the corresponding CV curves, which exhibit characteristics of both EDLC and pseudocapacitance. At a scan rate of 5 m*V* s^{-1}, well-defined redox couples appear at 0.925/0.932, 1.000/0.934, and 1.107/0.988 V for AQ-HATN, PQ-HATN, and DPED-HATN CMPs, respectively, arising from the reversible multi-electron redox activity of the HATN units. In addition, AQ-HATN and PQ-HATN CMP display additional broad redox features associated with quinone carbonyl redox processes, whereas this response is absent in DPED–HATN CMP, highlighting that substitution of quinone carbonyl groups with the benzil moiety containing aliphatic carbonyls suppresses the broad redox features.

Furthermore, as the scan rate increased from 5 to 100 mV s^{-1}, both cathodic and anodic current densities of the well-defined redox couples increased proportionally while the overall shape of the CV curves was retained, confirming the excellent redox reversibility of the HATN-based CMP electrodes [14–17]. Fig. 9**(d–f)** presents the GCD curves of the three HATN-based CMPs SSC device at current densities of 0.1, 0.2, 0.3, 0.4, 0.5, 0.6, 0.8, 1.0, and 1.5 A g^{-1}. The curves exhibit a pair of plateaus, consistent with the redox potentials observed in the CV curves. Moreover, the charge-discharge profiles are almost symmetrical, indicating that both HATN and carbonyl moieties possesses excellent electrochemical activity and that the energy storage process is highly reversible. The specific capacitance values derived from the GCD profiles (0–1.2 V) were determined by two methods: (i) for the overall symmetric device, using **Eq. (S4)**, with the results presented in Fig. 10 (a); and (ii) for a single electrode, using to **Eq. (S5)**, with the corresponding data provided in the Supporting Information (**Fig. S15**). This distinction is critical to ensure fair and accurate comparison with literature values, as some studies report device capacitance while others normalize to a single electrode. The specific capacitance values at 0.1 A g^{-1} are 174.07 ± 1.3, 92.3 ± 1.5, and 54.11 ± 1.2 F g^{-1} for AQ-HATN CMP//AQ-HATN CMP, PQ-HATN CMP//PQ-HATN CMP, and DPED-HATN CMP//DPED-HATN CMP SSC devices, respectively. Moreover, the Ragone plots in Fig. 10(b) demonstrate that the AQ-HATN CMP//AQ-HATN CMP device achieves a high energy density of 34.814 ± 0.3 Wh Kg^{-1} at 60 W Kg^{-1} (0.1 A g^{-1}). Fig. 10(c) shows the Nyquist plots of the AQ-HATN CMP//AQ-HATN CMP, PQ-HATN CMP//PQ-HATN CMP, and DPED-HATN CMP//DPED-HATN CMP SSC devices. The AQ-HATN CMP electrode exhibits the lowest R_s and R_{ct} values (1.960, 2.622 Ω, respectively; **Table S10**) at high frequencies, as well as the steepest low-frequency slope in the EIS profiles. These features indicate rapid interfacial charge-transfer and minimal ion diffusion resistance, highlighting the superior electrochemical kinetics of AQ-HATN CMP compared to the other electrodes. The Cyclability test of the AQ-HATN CMP//AQ-HATN CMP SSC device at 1 A g^{-1} (Fig. 10(d)) shows that the device delivered 100% Coulombic efficiency and capacitance retention over 10,000 cycles. Such remarkable stability (100%, 10,000) clearly outperforms previously reported SCs (**Table S11**). Notably, the last ten GCD curves (**inset of** Fig. 10(d)) remain nearly identical to the initial cycles, further confirming the ultra-long cycling life and robust retention of the electrode architecture. Similarly, **Fig. S16** and **Fig. S17** show the Cyclability test of PQ-HATN CMP and DPED-HATN CMP, respectively. Notably, the energy density of the AQ-HATN CMP//AQ-HATN CMP device is markedly outperforming the reported state-of-the-art quinone-based symmetric and asymmetric SC devices (Fig. 10(e) **and Table S11**), such as tetramino-benzoquinone (TABQ) with multi-walled carbon nanotubes (MWCNTs) (TABQ-MWCNTs, 15.7 Wh Kg^{-1} at 700 W Kg^{-1}) [88], nitrogen incorporated carbon sphere $(C_{\beta-CD/N-AQ})$ from β-cyclodextrin/N-amino-anthraquinone ($C_{\beta-CD/N-AQ}$, 21 at 500) [89], TABQ (14.1 at 100) [90], An-TPA POP (8.57 at 500) [29], DTCz-Pyz-AQ/GF (15.94 at 899.71) [46], Anthraquinone-modified porous carbon (1-AAQ-CC2, 14.8 at 240) [91], benzenetricarbaldehyde-2,6-diaminoanthraquinone-based COF (TpOMe-DAQ, 0.3 at 6.5) [92], RGO/PQ-1.5 (19.3 at 186.8) [36], BC-PT CMP (14.86 at 600) [34], CAT-AZO-AQ/GF (3.5 at 1080) [47], Hollow anthraquinone-based COF (Hollow COF-DAAQ-Tp, 17.8 at 604) [93].

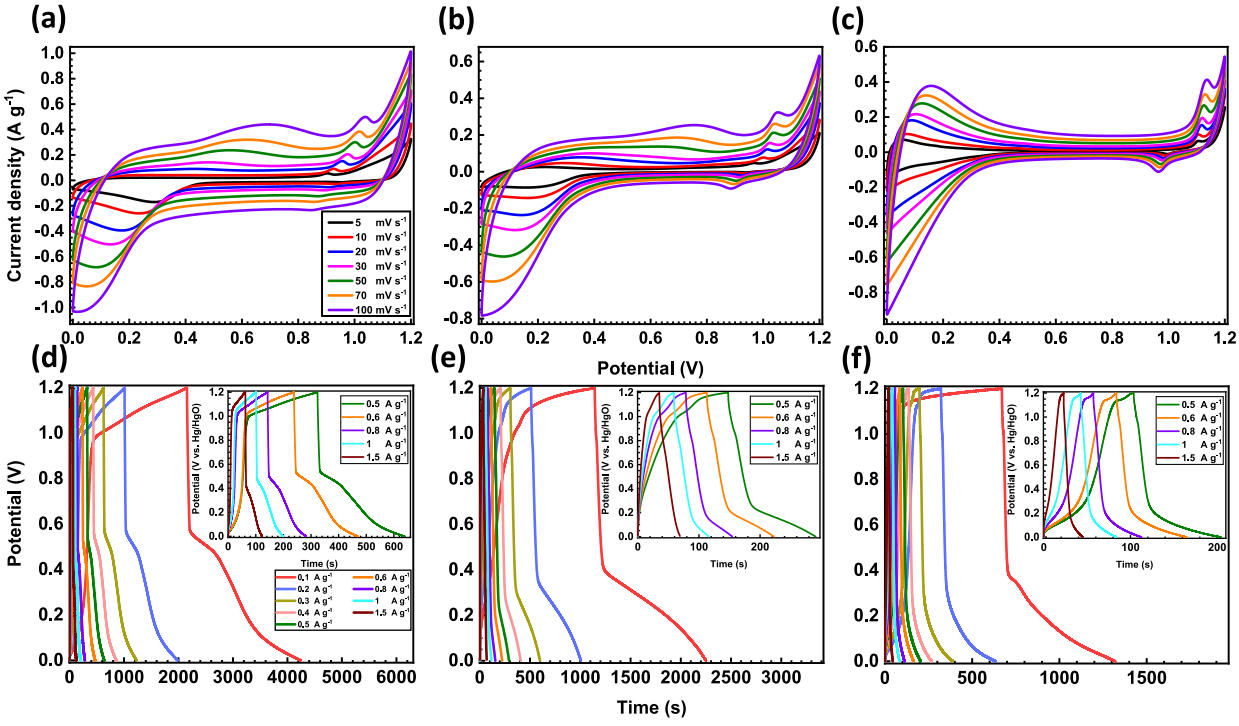

Fig. 9. CV curves (a–c) and GCD curves (d–f) of (a, d) AQ-HATN CMP//AQ-HATN CMP, (b, e) PQ-HATN CMP//PQ-HATN CMP, and (c, f) DPED-HATN CMP//DPED-HATN CMP devices recorded at various scans. Insets of (d–f) display magnified GCD curves at higher current densities.

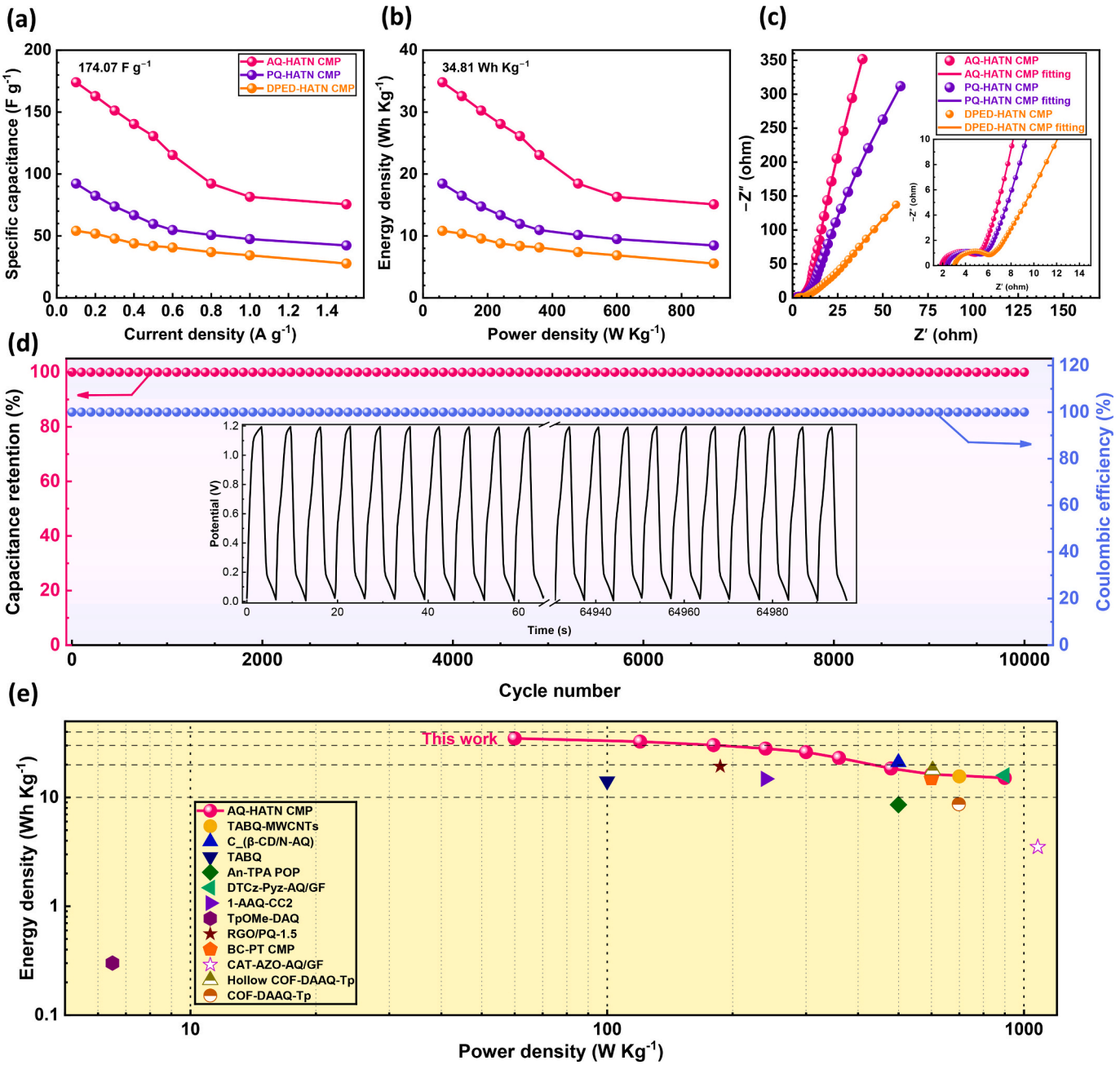

Fig. 10. (a) Specific capacitance, (b) Ragone plots, and (c) Nyquist plots and their fitted plots of AQ-HATN CMP//AQ-HATN CMP, PQ-HATN CMP//PQ-HATN CMP, and DPED-HATN CMP//DPED-HATN CMP devices, inset: High-frequency region. (d) Cycling stability of AQ-HATN CMP//AQ-HATN CMP at 1 A g^{-1}, inset: GCD profiles of AQ-HATN CMP//AQ-HATN CMP in the first and last ten cycles. (e) Comparative analysis of AQ-HATN CMP with previously reported redox-active polymers.

3.3. Density functional theory (DFT) and electrostatic potential analysis studies

DFT calculations were implemented to elucidate the electronic structures and charge distribution characteristics of the AQ, PQ, DPED, and HATN monomers, and to correlate these features with the electrochemical performances of their corresponding CMPs (**Fig. S18**). The highest occupied molecular orbital (HOMO) and lowest unoccupied molecular orbital (LUMO) energy levels for AQ (−7.00 and − 2.80 eV), PQ (−6.61 and − 2.98 eV), DPED (−6.42 and − 2.26 eV), and HATN (−6.40 and − 2.63 eV) indicate that AQ possesses the deepest HOMO, reflecting strong π-conjugation and favorable electron delocalization [23,50,90]. The LUMO levels of AQ (−2.80 eV) and PQ (−2.98 eV) lie below that of HATN (−2.63 eV), suggesting that electrons readily transfer from the HATN core to these carbonyl-based linkers, forming efficient donor–acceptor channels that enhance charge mobility [81,90]. Conversely, the higher LUMO of DPED (−2.26 eV) relative to HATN indicates that electron transfer occurs from DPED to HATN. For the HATN-based CMPs (Fig. 11), the HOMO density of AQ-HATN and PQ-HATN CMPs is mainly localized on the HATN moieties, whereas the LUMO density is concentrated on the quinone-type (AQ or PQ) moieties, confirming their intrinsic donor-acceptor nature [68]. This spatial separation of frontier orbitals modulates the surface electron density and forms well-defined, rapid ion-transport pathways from the HATN domains to the quinone (AQ or PQ) moieties, thereby enhancing intramolecular charge transfer and facilitating electron hopping across the

conjugated network. In contrast, both the HOMO and LUMO orbitals of DPED-HATN CMP are primarily delocalized over the HATN moieties, indicating the absence of donor–acceptor interactions and consequently reduced electronic transport efficiency [94]. The calculated HOMO–LUMO gaps follow the order DPED-HATN CMP (3.38 eV) > AQ-HATN CMP (3.27 eV) > PQ-HATN CMP (3.17 eV), implying that PQ-HATN CMP should exhibit the highest intrinsic conductivity [90]. However, electrochemical measurements reveal that AQ-HATN CMP delivers the superior specific capacitance and rate performance. This apparent discrepancy highlights that charge-storage efficiency is not solely determined by bandgap narrowing, but rather by the extent of orbital delocalization and the accessibility of redox-active sites.

Molecular electrostatic potential (MESP) mapping (Fig. 12 **and Fig. S19**) further elucidates the relationship between electronic structure and ion-binding capability. The most negative regions of the MESP surfaces correspond to nucleophilic sites that preferentially interact with cations during the charge–discharge process. Red regions indicate high electron density, while blue areas represent electron-deficient zones. Among the monomers, the lone pairs on the nitrogen atoms of HATN and the two oxygen atoms of PQ exhibit the most negative electrostatic potentials (−49 kcal mol^{-1}). The oxygen atoms in DPED and AQ show less negative potentials of −32 and − 31 kcal mol^{-1}, respectively. For the HATN-based CMPs (Fig. 12), the electrostatic potential at the C═N sites of HATN slightly decreases from −49 to −47, −46, and − 48 kcal mol^{-1} in AQ-, PQ-, and DPED-HATN CMPs, respectively, while the ESP at the C═O sites of PQ becomes even more negative (from −49 to −50 kcal mol^{-1}). The presence of both carbonyl groups on the same side of the PQ molecule enhances its local electron-withdrawing character. Although PQ-HATN exhibits the most negative potential at its C═O sites, this originates from localized electron accumulation caused by the sterically congested *peri*-diketone configuration, which disrupts molecular planarity and limits π-conjugation. In contrast, AQ-HATN displays moderately negative but uniformly distributed potentials across both C═O and C═N sites, indicating a higher degree of electron delocalization and stronger intraframework electronic coupling throughout the conjugated network. Such delocalization reduces localized charge density over redox-active sites (C═O and C═N groups), thereby weakening ion-site interactions and enabling faster ion diffusion through the CMP networks. DPED-HATN shows intermediate potentials values, consistent with its *vicinal* carbonyl geometry, which partially interrupts π-conjugation and restricts delocalization.

Overall, the systematic engineering of carbonyl positioning within the AQ-, PQ-, and DPED-HATN CMP frameworks demonstrates a profound structure–property correlation across multiple scales. The *para*-diketone configuration in AQ promotes molecular planarity and extended π-conjugation, leading to a well-interconnected micro–mesoporous network with the highest surface area and uniform rod-like structures. This structural order enhances electron delocalization, facilitates rapid ion transport, and results in the superior capacitance and rate capability of AQ-HATN CMP. In contrast, the *peri*-diketone arrangement in PQ introduces strong steric and electronic repulsion between adjacent carbonyl groups, distorting planarity and producing irregularly aggregated morphologies with broader pore distributions. Although PQ-HATN exhibits highly negative local electrostatic potentials, its localized electron accumulation and disrupted conjugation hinder charge mobility and ion accessibility, yielding inferior electrochemical performance. The *vicinal*-diketone configuration in DPED combines electron-withdrawing and steric effects, generating moderate porosity and partial conjugation, thus producing intermediate performance. Collectively, the XPS, textural, morphological, and DFT analyses demonstrate that carbonyl position engineering plays a decisive role in governing framework planarity, pore hierarchy, charge delocalization, and ion diffusion pathways–ultimately dictating the electrochemical performance of HATN-based CMP electrodes. These findings provide molecular-level insights for the rational design of next-generation redox-active conjugated microporous polymers through precise carbonyl positioning and electronic structure modulation.

4. Conclusion

In summary, a series of redox-active hexaazatrinaphthalene-based conjugated microporous polymers (CMPs)–AQ-HATN, PQ-HATN, and DPED-HATN–were successfully designed and synthesized via Suzuki–Miyaura coupling to investigate the effect of carbonyl positioning on charge-storage behavior. The systematic variation in the position and conjugation geometry of carbonyl groups enabled fine-tuning of the electronic structure, surface area, pore architecture, redox potential, and electrochemical performance. Among the three CMPs, AQ-HATN exhibited the highest specific capacitance in the three-electrode configuration (543.4 F g^{-1} at 0.5 A g^{-1}) and outstanding cycling stability (96.2% retention after 10,000 cycles), outperforming PQ-HATN and DPED-HATN. The symmetric device AQ-HATN CMP//AQ-HATN CMP delivers a total capacitance of 174.07 ± 1.3 F g^{-1} (328.14 ± 2.6 F g^{-1} per electrode) at 0.1 A g^{-1}, an energy density of 34.8 ± 0.3 Wh Kg^{-1} at 60 W Kg^{-1}. It maintains nearly 100% capacitance retention and Coulombic efficiency over 10,000 cycles at 1 A g^{-1}. The superior performance of AQ-HATN CMP arises from its *para*-diketone configuration, which promotes extended π-conjugation, balanced donor–acceptor coupling, and homogeneous charge delocalization. In contrast, the *peri*-diketone PQ and *ortho*-diketone DPED linkers introduce steric and electronic constraints that hinder orbital overlap and slow charge-transfer kinetics. DFT and molecular electrostatic potential analyses corroborate these experimental findings, revealing that optimal redox behavior depends not solely on a narrow bandgap but on balanced electronic coupling and delocalized frontier orbitals. This work highlights carbonyl-position engineering as a powerful molecular strategy for tailoring redox properties and advancing the rational design of high-performance organic supercapacitor electrodes.

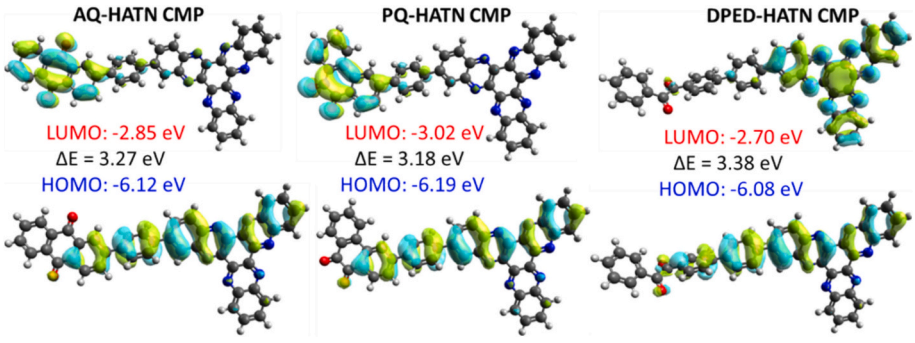

Fig. 11. HOMO and LUMO isosurface maps of the AQ-HATN, PHTD-HATN, and BPED HATN CMPs, their energies, and the HOMO-LUMO gap calculated at the B3LYP-D3(BJ)/6-31G(d) level.

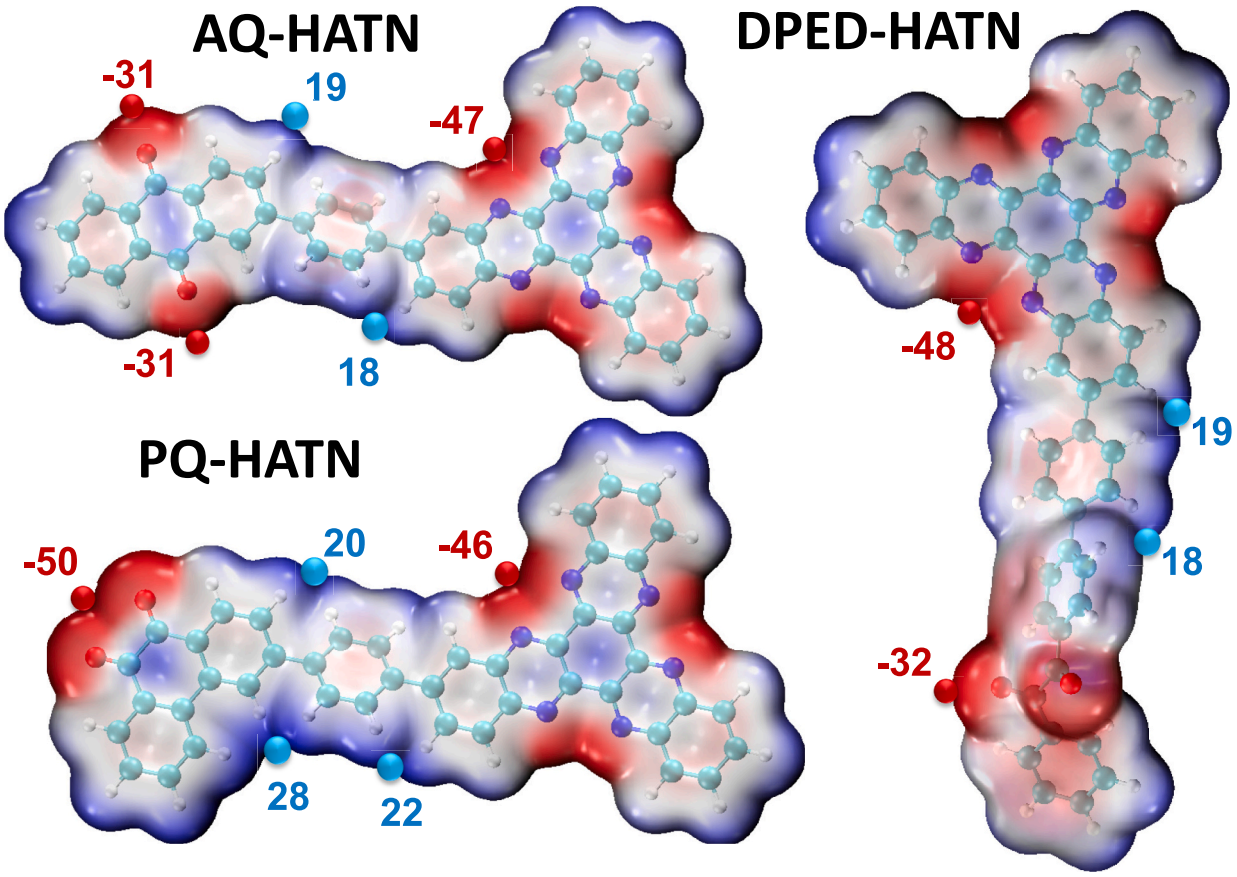

Fig. 12. Molecular electrostatic potential (MESP) surfaces of AQ-HATN, PQ-HATN, and DPED-HATN CMPs, showing ESP maxima and minima (in kcal mol^{-1}) calculated at the B3LYP-D3(BJ)/6-31G(d) level.

CRediT authorship contribution statement

Aya Farouk Farghal: Writing – review & editing, Writing – original draft, Investigation, Formal analysis, Data curation, Conceptualization. **Tharwat H. Mansoure:** Writing – review & editing, Writing – original draft, Formal analysis, Data curation. **Mohamed Gamal Mohamed:** Writing – review & editing, Writing – original draft, Supervision, Methodology, Investigation, Formal analysis, Data curation, Conceptualization. **Ahmed A.K. Mohammed:** Software. **Shiao-Wei Kuo:** Supervision, Resources, Project administration.

Declaration of competing interest

The authors declare that they have no known competing financial interests or personal relationships that could have appeared to influence the work reported in this paper.

Acknowledgments

This study was supported financially by the National Science and Technology Council, Taiwan, under contracts NSTC 114-2223-E-110-001- and 113-2221-E-110-012-MY3. The authors thank the staff at National Sun Yat-sen University for their assistance with the TEM (ID: EM022600) experiments.

Appendix A. Supplementary data

Supplementary data to this article can be found online at https://doi.org/10.1016/j.cej.2026.174848.

Data availability

Data will be made available on request.

References

[1] J. Chang, Y. Yang, Recent advances in zinc-air batteries: self-standing inorganic nanoporous metal films as air cathodes, Chem. Commun. 59 (2023) 5823–5838, https://doi.org/10.1039/D3CC00742A.
[2] J. Baigorri, F. Zaversky, D. Astrain, Massive grid-scale energy storage for next-generation concentrated solar power: a review of the potential emerging concepts, Renew. Sust. Energ. Rev. 185 (2023) 113633, https://doi.org/10.1016/J.RSER.2023.113633.
[3] H. Chen, Y. Zheng, J. Li, L. Li, X. Wang, AI for nanomaterials development in clean energy and carbon capture, utilization and storage (CCUS), ACS Nano 17 (2023) 9763–9792, https://doi.org/10.1021/ACSNANO.3C01062.
[4] J.D. Hunt, J. Jurasz, B. Zakeri, W. Tong, A. Nascimento, F. Guo, B. Đurin, P. Dąbek, Y. Wada, B. van Ruijven, K. Riahi, Electric truck gravity energy storage: An alternative to seasonal energy storage, Energy Storage 6 (2024) e575, https://doi.org/10.1002/EST2.575.
[5] S.X. Liao, A.F.M. EL-Mahdy, Redox-active conjugated microporous polymers featuring a precise pore size for high-performance supercapacitor energy storage, ACS Appl. Energy Mater. 8 (2025) 3074–3086, https://doi.org/10.1021/ACSAEM.4C03232.
[6] A. Osama Mousa, S.U. Sharma, S.V. Chaganti, T.H. Mansoure, P.N. Singh, M. Ejaz, C.H. Chuang, J.T. Lee, S.W. Kuo, M.G. Mohamed, Designing strategically functionalized conjugated microporous polymers with pyrene and perylenetetracarboxylic dianhydride moieties with single-walled carbon nanotubes to enhance supercapacitive energy storage efficiency, J. Power Sources 608 (2024) 234624, https://doi.org/10.1016/J.JPOWSOUR.2024.234624.
[7] M.G. Mohamed, B. Halder, P.N. Singh, A.A.K. Mohammed, P. Elumalai, S.W. Kuo, Molecular engineering and synergistic redox-active hexaazatrinaphthalene and pyrene-based conjugated microporous polymers for superior faradaic supercapacitor energy storage, Chem. Eng. J. 520 (2025) 165892, https://doi.org/10.1016/J.CEJ.2025.165892.
[8] X. Pan, Z. Supiyeva, Z. Wang, Q. Abbas, Progress and challenges of zinc ion capacitors: from basic principles to performance optimization strategies, Chem. Eng. J. 516 (2025) 163974, https://doi.org/10.1016/J.CEJ.2025.163974.

[9] S.V. Bhosale, S.V. Bhosale, Advancements in supercapacitors: breaking barriers and enabling amazing applications, Chem. Sci. 16 (2025) 10159, https://doi.org/10.1039/D5SC01955A.

[10] R. Jaryal, B.B. Upreti, P. Kumar, S. Sutradhar, S. Khullar, R.S. Dey, R. Kumar, Unveiling the charge storage mechanism of a supercapacitor constructed from an ortho-quinone-derived covalent organic framework on electrophoretically exfoliated graphene, J. Mater. Chem. A 12 (2024) 23076–23086, https://doi.org/10.1039/D4TA01917B.

[11] S.P. Ega, S.N. Karri, P. Srinivasan, High-performance with a high voltage aqueous supercapacitor cell from a simple hybrid electrode of manganese oxide-phenanthrenequinone-graphite sheet, J. Energy Storage 56 (2022) 106038, https://doi.org/10.1016/J.EST.2022.106038.

[12] M.G. Mohamed, S.V. Chaganti, S.U. Sharma, M.M. Samy, M. Ejaz, J.T. Lee, K. Zhang, S.W. Kuo, Constructing conjugated microporous polymers containing the Pyrene-4,5,9,10-Tetraone unit for energy storage, ACS Appl. Energy Mater. 5 (2022) 10130–10140, https://doi.org/10.1021/ACSAEM.2C01842.

[13] K. Zou, W. Deng, D.S. Silvester, G. Zou, H. Hou, C.E. Banks, L. Li, J. Hu, X. Ji, Carbonyl chemistry for advanced electrochemical energy storage systems, ACS Nano 18 (2024) 19950–20000, https://doi.org/10.1021/ACSNANO.4C02307.

[14] K. Amin, N. Ashraf, L. Mao, C.F.J. Faul, Z. Wei, Conjugated microporous polymers for energy storage: recent progress and challenges, Nano Energy 85 (2021) 105958, https://doi.org/10.1016/J.NANOEN.2021.105958.

[15] S. Luo, Z. Zeng, H. Wang, W. Xiong, B. Song, C. Zhou, A. Duan, X. Tan, Q. He, G. Zeng, Z. Liu, R. Xiao, Recent progress in conjugated microporous polymers for clean energy: synthesis, modification, computer simulations, and applications, Prog. Polym. Sci. 115 (2021) 101374, https://doi.org/10.1016/J.PROGPOLYMSCI.2021.101374.

[16] H. Liu, L. Teng, W. He, J. Duan, X. Gong, X. Mi, Y. Zhuang, B. Sun, W. Lyu, Y. Liao, Synergistic modulation of band gap and porosity in conjugated microporous polymers for high-rate Lithium-ion storage, ACS Appl. Energy Mater. 8 (2025) 9760–9769, https://doi.org/10.1021/ACSAEM.5C01112.

[17] D. Zhou, K. Zhang, S. Zou, X. Li, H. Ma, Conjugated microporous polymers: their synthesis and potential applications in flexible electrodes, J. Mater. Chem. 12 (2024) 17021, https://doi.org/10.1039/D4TA02085E.

[18] A. Hayat, M. Sohail, A. El Jery, K.M. Al-Zaydi, S. Raza, H. Ali, Y. Al-Hadeethi, T. A. Taha, I. Ud Din, M. Ali Khan, M.A. Amin, E. Ghasali, Y. Orooji, Z. Ajmal, M. Zahid Ansari, Recent advances in ground-breaking conjugated microporous polymers-based materials, their synthesis, modification and potential applications, Mater. Today 64 (2023) 180–208, https://doi.org/10.1016/J.MATTOD.2023.02.025.

[19] Z. Zhao, B. Wang, Z. You, Q. Zhang, W. Song, X. Long, Z. Zhao, B. Wang, Z. You, Q. Zhang, W. Song, X. Long, Heterocyclic modulated electronic states of Alkynyl-containing conjugated microporous polymers for efficient oxygen reduction, Small 19 (2023) 2207298, https://doi.org/10.1002/SMLL.202207298.

[20] H. Xu, R. Liu, Z. Chen, J. Liu, X. Bai, K. Cai, X. Li, Design and synthesis of carbazole-based conjugated microporous polymers for CO2 capture, Sep. Purif. Technol. 359 (2025) 130449, https://doi.org/10.1016/J.SEPPUR.2024.130449.

[21] Y. Lei, Z. Li, S. Wang, Y. Jiang, B. Chai, M. Cui, Y. Guo, Y. Li, J. xin Ma, L. Zhao, Monolithic polar conjugated microporous polymers: optimisation of adsorption capacity and permeability trade-off based on process simulation of flue gas separation, Chem. Eng. J. 495 (2024) 153538, https://doi.org/10.1016/J.CEJ.2024.153538.

[22] M.G. Mohamed, I.M.A. Mekhemer, A.F.H. Selim, A. Katsamitros, D. Tasis, A. Basit, H.H. Chou, S.W. Kuo, Molecular engineering of donor–acceptor-type conjugated microporous polymers for dual effective photocatalytic production of hydrogen and hydrogen peroxide, Mater. Horiz. 12 (2025) 5917–5928, https://doi.org/10.1039/D5MH00735F.

[23] X. Xu, J. Liu, Y. Sun, Z. Li, Molecular engineering of novel D−A1−A2 conjugated microporous polymers by efficient electron donor for highly enhanced photocatalytic hydrogen generation, Sep. Purif. Technol. 364 (2025) 132454, https://doi.org/10.1016/J.SEPPUR.2025.132454.

[24] Y. Liu, Y. Lu, Y. Hou, X. Xiao, H. Yue, X. Liu, Fully conjugated microporous polymers as metal-free heterogeneous Photocatalysts for organic transformations, Macromol. Rapid Commun. 46 (2025) 2400743, https://doi.org/10.1002/MARC.202400743.

[25] J. Zhang, X. Zhou, H. Mao, Z. Yang, J. Zhang, L. Xu, J. Zhuang, Conjugated microporous polymer Nanosheets functionalized with TEMPO radicals as efficient heterogeneous catalysts for selective aerobic oxidation of alcohols, ACS Appl. Polym. Mater. 7 (2025) 2567–2575, https://doi.org/10.1021/ACSAPM.4C03825.

[26] B. Reis, R. Frenzel, N. Gerlach, M. Müller, J. Schultz, S. Putwa, J. Weatherby, M. Dasog, S. Schwarz, Gold Nanorods decorated by conjugated microporous polymers for infrared responsive cytostatic drug delivery, Langmuir 41 (2025) 2471–2479, https://doi.org/10.1021/ACS.LANGMUIR.4C04164.

[27] M.G. Mohamed, A. Basit, M. Madhu, K. Aravinthkumar, A.I. Said, D. Manoj, W. L. Tseng, S.W. Kuo, Conjugated microporous polymer containing pyrene and dibenzo[g,p]chrysene moieties as a luminescent powerhouse for multi-target sensing and environmental safety, Microporous Mesoporous Mater. 391 (2025) 113620, https://doi.org/10.1016/J.MICROMESO.2025.113620.

[28] A. Chougle, A. Rezk, S.U. Bin Afzal, A.K. Mohammed, D. Shetty, A. Nayfeh, Evolving role of conjugated polymers in nanoelectronics and photonics, Nano Micro Lett. 17 (2025) 1–30, https://doi.org/10.1007/S40820-025-01748-7, 1 17 (2025).

[29] A.F. Saber, S. Abdelnaser, A.F.M. EL-Mahdy, S.W. Kuo, One-pot synthesis of heteroatom-rich anthraquinone-based benzoxazine-linked porous organic polymers for high performance supercapacitors, Electrochim. Acta 511 (2025) 145397, https://doi.org/10.1016/J.ELECTACTA.2024.145397.

[30] D. Tang, C. Lin, X. Lou, M. Yin, T. Qiu, J. Chen, Tunable synthesis of conjugated microporous polymers and their adsorption performance toward heavy metals, Macromol. Chem. Phys. 226 (2025) 2400533, https://doi.org/10.1002/MACP.202400533.

[31] H. Ali, O. Iqbal, M. Sadiq, Y. Cheng, X. Yan, B. Al Alwan, A. El Jery, H. ur Rahman, Y. Qian, A. Hayat, D. Yue, Z. Ajmal, Novel advancements in synthesis, modulation, and potential applications of conjugated microporous polymer-based materials, Nano Mater. Sci. (2025), https://doi.org/10.1016/J.NANOMS.2024.08.008.

[32] D.M. Anjos, J.K. McDonough, E. Perre, G.M. Brown, S.H. Overbury, Y. Gogotsi, V. Presser, Pseudocapacitance and performance stability of quinone-coated carbon onions, Nano Energy 2 (2013) 702–712, https://doi.org/10.1016/J.NANOEN.2013.08.003.

[33] M. Li, J. Liu, Y. Li, G. Xing, X. Yu, C. Peng, L. Chen, Skeleton engineering of isostructural 2D covalent organic frameworks: Orthoquinone redox-active sites enhanced energy storage, CCS Chem. 3 (2021) 696–706, https://doi.org/10.31635/CCSCHEM.020.202000257.

[34] A.F. Saber, Y.F. Chen, L. Mabuti, S.V. Chaganti, S.U. Sharma, J. Lüder, J.T. Lee, S. W. Kuo, A.F.M. EL-Mahdy, Engineering carbonyl-rich conjugated microporous polymers with a pyrene-4,5,9,10-tetraone building block as highly efficient and stable electrodes for energy storage, Mater. Adv. 6 (2025) 607–616, https://doi.org/10.1039/D4MA00928B.

[35] L. Sun, W. Zhang, Z. Gu, X. Li, H. Kang, Z. Li, B. Yang, Rational design of hierarchical porous reduced graphene oxide/9,10-phenanthraquinone/porous carbon nanocomposites for high-performance supercapacitors, Electrochim. Acta 493 (2024) 144408, https://doi.org/10.1016/J.ELECTACTA.2024.144408.

[36] W. Zhang, H. Liu, L. Sun, Z. Li, H. Kang, Z. Li, B. Yang, Redox-active 9,10-phenanthrenequinone non-covalently modify reduced graphene oxide for high-performance asymmetric supercapacitor and zinc-ion hybrid capacitors, J. Energy Storage 75 (2024) 109649, https://doi.org/10.1016/J.EST.2023.109649.

[37] X. Chen, H. Wang, H. Yi, X. Wang, X. Yan, Z. Guo, Anthraquinone on porous carbon nanotubes with improved supercapacitor performance, J. Phys. Chem. C 118 (2014) 8262–8270, https://doi.org/10.1021/JP5009626.

[38] C.R. Deblase, K.E. Silberstein, T.T. Truong, H.D. Abruña, W.R. Dichtel, B-Ketoenamine-linked covalent organic frameworks capable of pseudocapacitive energy storage, J. Am. Chem. Soc. 135 (2013) 16821–16824, https://doi.org/10.1021/JA409421D.

[39] Y. Yang, D. Xu, Q. Sun, Y. Li, W. Zhang, Z. Li, Z. Hu, Anthraquinone-based covalent organic framework/reduced graphene oxide composites for supercapacitors, J. Energy Storage 114 (2025) 115881, https://doi.org/10.1016/J.EST.2025.115881.

[40] B. Häupler, A. Wild, U.S. Schubert, B. Häupler, A. Wild, U.S. Schubert, Carbonyls: powerful organic materials for secondary batteries, Adv. Energy Mater. 5 (2015) 1402034, https://doi.org/10.1002/AENM.201402034.

[41] Q. Zhao, W. Huang, Z. Luo, L. Liu, Y. Lu, Y. Li, L. Li, J. Hu, H. Ma, J. Chen, High-capacity aqueous zinc batteries using sustainable quinone electrodes, Sci. Adv. 4 (2018), https://doi.org/10.1126/SCIADV.AAO1761.

[42] S. Abdelnaser, S.W. Kuo, A.F.M. EL-Mahdy, Conjugated microporous polymers incorporating pyridine moieties for efficient faradaic supercapacitor energy storage, J. Power Sources 635 (2025) 236535, https://doi.org/10.1016/J.JPOWSOUR.2025.236535.

[43] W. Yang, B. Huang, L. Li, K. Zhang, Y. Li, J. Huang, X. Tang, T. Hu, K. Yuan, Y. Chen, W. Yang, B. Huang, L. Li, K. Zhang, Y. Li, J. Huang, X. Tang, K. Yuan, Y. Chen, T. Hu, Covalently sandwiching MXene by conjugated microporous polymers with excellent stability for supercapacitors, Small Methods 4 (2020) 2000434, https://doi.org/10.1002/SMTD.202000434.

[44] X. Wu, B. Huang, Q. Wang, Y. Wang, Thermally chargeable supercapacitor using a conjugated conducting polymer: insight into the mechanism of charge-discharge cycle, Chem. Eng. J. 373 (2019) 493–500, https://doi.org/10.1016/J.CEJ.2019.05.075.

[45] T. Wang, S. Hu, W. Yu, Y. Hu, S. Yan, M. Wang, W. Zhao, J. Xu, J. Zhang, Biologically inspired small herbal biomolecules and biomass carbon for high-performance supercapacitors, ACS Appl. Energy Mater. 6 (2023) 2347–2357, https://doi.org/10.1021/ACSAEM.2C03544.

[46] S.D. Ambore, C.R.K. Rao, S.V. Bhosale, S.V. Bhosale, Donor–acceptor molecular architecture involving carbazole/pyrazine/anthraquinone units for efficient supercapacitor applications, Chem. Commun. 59 (2023) 10384–10387, https://doi.org/10.1039/D3CC03233G.

[47] S.D. Jagadale, S.V. Bhosale, S.V. Bhosale, High-performance flexible supercapacitor device based on catechol functionalized azo-anthraquinone, J. Power Sources 647 (2025) 237338, https://doi.org/10.1016/J.JPOWSOUR.2025.237338.

[48] H. Zhao, Y. Wang, R. Liu, W. Cheng, Y. Wu, H. Cao, F. Liang, Preparation and electrochemical properties of porous organic polymer with high ionic diffusion coefficient as cathode material for lithium-ion batteries, J. Power Sources 626 (2025) 235733, https://doi.org/10.1016/J.JPOWSOUR.2024.235733.

[49] J. Wang, J.C.Z. En, S.N. Riduan, Y. Zhang, Nitrogen-linked Hexaazatrinaphthylene polymer as cathode material in Lithium-ion battery, Chem. – A Eur. J. 26 (2020) 2581–2585, https://doi.org/10.1002/CHEM.201904773.

[50] J. Wang, K. Tee, Y. Lee, S.N. Riduane, Y. Zhang, Hexaazatriphenylene derivatives/GO composites as organic cathodes for lithium ion batteries, J. Mater. Chem. A 6 (2018) 2752, https://doi.org/10.1039/C7TA10232A.

[51] J.L. Segura, R. Juárez, M. Ramos, C. Seoane, Hexaazatriphenylene (HAT) derivatives: from synthesis to molecular design, self-organization and device applications, Chem. Soc. Rev. 44 (2015) 6850, https://doi.org/10.1039/C5CS00181A.

[52] J. Weng, Q. Xi, X. Zeng, Z.Q. Lin, J. Zhao, L. Zhang, W. Huang, Recent Progress of Hexaazatriphenylene-based electrode materials for rechargeable batteries, Catal. Today 400–401 (2022) 102–114, https://doi.org/10.1016/J.CATTOD.2021.09.040.

[53] M.G. Mohamed, S.U. Sharma, C.H. Yang, M.M. Samy, A.A.K. Mohammed, S. V. Chaganti, J.T. Lee, S. Wei-Kuo, Anthraquinone-enriched conjugated microporous polymers as organic cathode materials for high-performance Lithium-ion batteries, ACS Appl. Energy Mater. 4 (2021) 14628–14639, https://doi.org/10.1021/ACSAEM.1C03270.

[54] S. Li, Y. Liu, L. Dai, S. Li, B. Wang, J. Xie, P. Li, A stable covalent organic framework cathode enables ultra-long cycle life for alkali and multivalent metal rechargeable batteries, Energy Storage Mater. 48 (2022) 439–446, https://doi.org/10.1016/J.ENSM.2022.03.033.

[55] Y.C. Kao, K.T. Yeh, M.G. Mohamed, H. Karim, W.H. Su, S.W. Kuo, Structural modulation via mesoporous silica templating in covalent organic frameworks: converting functional aspects for adsorption behavior, Sep. Purif. Technol. 375 (2025) 133827, https://doi.org/10.1016/J.SEPPUR.2025.133827.

[56] K. Li, Q. Liu, H. Cheng, M. Hu, S. Zhang, Classification and carbon structural transformation from anthracite to natural coaly graphite by XRD, Raman spectroscopy, and HRTEM, Spectrochim. Acta A Mol. Biomol. Spectrosc. 249 (2021) 119286, https://doi.org/10.1016/J.SAA.2020.119286.

[57] F. Astuti, N. Sari, V.L. Maghfirohtuzzoimah, R. Asih, M.A. Baqiya, D. Darminto, Study of the formation of amorphous carbon and rGO-like phases from Palmyra sugar by variation of calcination temperature, J. Fis. Dan Apl. 16 (2020) 91, https://doi.org/10.12962/J24604682.V16I2.6706.

[58] Y. Liu, L. Cao, J. Luo, Y. Peng, Q. Ji, J. Dai, J. Zhu, X. Liu, Biobased nitrogen- and oxygen-Codoped carbon materials for high-performance supercapacitor, ACS Sustain. Chem. Eng. 7 (2019) 2763–2773, https://doi.org/10.1021/ACSSUSCHEMENG.8B05947.

[59] M. Ejaz, M.G. Mohamed, Y.T. Chen, K. Zhang, S.W. Kuo, Porous carbon materials augmented with heteroatoms derived from hyperbranched biobased benzoxazine resins for enhanced CO_2 adsorption and exceptional supercapacitor performance, J. Energy Storage 78 (2024) 110166, https://doi.org/10.1016/J.EST.2023.110166.

[60] L. Teng, J. Duan, H. Liu, X. Zhang, J. Li, Y. Li, J. Hong, W. Lyu, Y. Liao, A conjugated microporous polymer–graphene composite porous sandwich-like film for highly efficient flexible supercapacitors, J. Mater. Chem. A 12 (2024) 12423–12434, https://doi.org/10.1039/D4TA01603C.

[61] Y. Liao, H. Wang, M. Zhu, A. Thomas, Y. Liao, H. Wang, M. Zhu, A. Thomas, Efficient supercapacitor energy storage using conjugated microporous polymer networks synthesized from Buchwald–Hartwig coupling, Adv. Mater. 30 (2018) 1705710, https://doi.org/10.1002/ADMA.201705710.

[62] I.M.A. Mekhemer, A.M. Elewa, M.M. Elsenety, M.M. Samy, M.G. Mohamed, A. F. Musa, T.F. Huang, T.C. Wei, S.W. Kuo, B.H. Chen, S. Da Yang, H.H. Chou, Self-condensation for enhancing the hydrophilicity of covalent organic polymers and photocatalytic hydrogen generation with unprecedented apparent quantum yield up to 500 nm, Chem. Eng. J. 497 (2024) 154280, https://doi.org/10.1016/J.CEJ.2024.154280.

[63] A. Basit, M.G. Mohamed, S.U. Sharma, S.W. Kuo, Thianthrene- and Thianthrene Tetraoxide-functionalized conjugated microporous polymers for efficient energy storage, ACS Appl. Polym. Mater. 6 (2024) 12247–12260, https://doi.org/10.1021/ACSAPM.4C02368.

[64] A. Basit, Y.C. Kao, Y.A. El-Ossaily, S.W. Kuo, M.G. Mohamed, Rational engineering and synthesis of pyrene and thiazolo[5,4-d]thiazole-functionalized conjugated microporous polymers for efficient supercapacitor energy storage, J. Mater. Chem. A 12 (2024) 30508–30521, https://doi.org/10.1039/D4TA05908E.

[65] Y.M. Nabil, S. Abdelnaser, A.A.K. Mohammed, S.W. Kuo, A.F.M. EL-Mahdy, Engineering redox-active benzo[1,2-b :4,5-b ′]dithiophene-based conjugated polymers: tuning porosity and linker architecture for high-performance supercapacitors, J. Mater. Chem. A 13 (2025) 26337–26349, https://doi.org/10.1039/D5TA03907J.

[66] P. Xu, S. Ouyang, Q. Bai, Q. Ma, Y. Zhu, A hexaazatriphenylene-based porous organic polymer for high performance supercapacitor, J. Polym. Sci. 62 (2024) 1647–1653, https://doi.org/10.1002/POL.20230256.

[67] X. Li, Z. Li, Y. Zhang, H. Guo, M. Zou, H. Li, Y. Liu, S. Liu, Stable hexaazatrinaphthylene-based covalent organic framework as high-capacity electrodes for aqueous hybrid supercapacitors, Energy Materials 5 (2025) 500036, 5 (2025) N/A-N/A, 10.20517/ENERGYMATER.2024.127.

[68] F. Lu, Y. Che, H. Tian, Y. Cai, Q. Kong, X. Yao, Z. Su, Anthraquinone-based conjugated microporous polymer as anode for Long-life Lithium batteries, ACS Appl. Polym. Mater. 6 (2024) 15114–15123, https://doi.org/10.1021/ACSAPM.4C02652.

[69] M.M. Rahman, M. Muttakin, A. Pal, A.Z. Shafiullah, B.B. Saha, A statistical approach to determine optimal models for IUPAC-classified adsorption isotherms, Energies Vol. 12 (2019), https://doi.org/10.3390/EN12234565. Page 4565 12 (2019) 4565.

[70] M. Thommes, K. Kaneko, A.V. Neimark, J.P. Olivier, F. Rodriguez-Reinoso, J. Rouquerol, K.S.W. Sing, Physisorption of gases, with special reference to the evaluation of surface area and pore size distribution (IUPAC technical report), Pure Appl. Chem. 87 (2015) 1051–1069, https://doi.org/10.1515/PAC-2014-1117.

[71] L. Desmurs, A. Galarneau, C. Cammarano, V. Hulea, C. Vaulot, H. Nouali, B. Lebeau, T.J. Daou, C. Vieira Soares, G. Maurin, M. Haranczyk, I. Batonneau-Gener, A. Sachse, Determination of microporous and mesoporous surface areas and volumes of mesoporous zeolites by corrected t-plot analysis, ChemNanoMat 8 (2022) e202200051, https://doi.org/10.1002/CNMA.202200051.

[72] D. Wang, V. Schramm, J. Pool, E. Pardali, A. Brandenburg, I.M.C.M. Rietjens, P. J. Boogaard, The effect of alkyl substitution on the oxidative metabolism and mutagenicity of phenanthrene, Arch. Toxicol. 96 (2022) 1109–1131, https://doi.org/10.1007/S00204-022-03239-9.

[73] M. Pittelkow, U. Boas, M. Jessing, K.J. Jensen, J.B. Christensen, Role of the peri -effect in synthesis and reactivity of highly substituted naphthaldehydes : a novel backbone amide linker for solid-phase synthesis, Org. Biomol. Chem. 3 (2005) 508–514, https://doi.org/10.1039/B412971G.

[74] N. Wazzan, Phenanthrenequinone (PQ)-based cathodes for lithium-ion batteries (LIBs): DFT insights into the role of NO2 position on electrochemical performance, J. Saudi Chem. Soc. 29 (2025) 1–12, https://doi.org/10.1007/S44442-025-00019-9.

[75] S.K.J. Shaikh, R.R. Kamble, P.K. Bayannavar, M.Y. Karidduraganavar, Benzils: a review on their synthesis, Asian J. Org. Chem. 11 (2022) e202100650, https://doi.org/10.1002/AJOC.202100650.

[76] Z. Pawelka, A. Koll, T. Zeegers-Huyskens, Solvent effect on the conformation of Benzil, J. Mol. Struct. 597 (2001) 57–66, https://doi.org/10.1016/S0022-2860(01)00593-2.

[77] M. Hanif, L. Ping, G. Cheng, W. Zhi-ming, Y. Shu-min, Y. Bing, W. Chun-lei, M. Yu-guang, Molecular properties of 9,10-phenanthrenequinone and benzil, Chem. Res. Chin. Univ. 25 (2009) 950–956. https://crcu.jlu.edu.cn/EN/Y2009/V25/I6/950.

[78] S.Y. Park, C.W. Kang, S.M. Lee, H.J. Kim, Y.J. Ko, J. Choi, S.U. Son, Nanoparticulate conjugated microporous polymer with post-modified Benzils for enhanced Pseudocapacitor performance, Chem. – A Eur. J. 26 (2020) 12343–12348, https://doi.org/10.1002/CHEM.202002311.

[79] L. Miao, L. Liu, Z. Shang, Y. Li, Y. Lu, F. Cheng, J. Chen, The structure–electrochemical property relationship of quinone electrodes for lithium-ion batteries, Phys. Chem. Chem. Phys. 20 (2018) 13478–13484, https://doi.org/10.1039/C8CP00597D.

[80] Q. Bai, J. Huang, K. Tang, Y. Zhu, D. Wu, Arylamine-linked porous organic polymers with abundant redox-active sites as high-capacity and high-rate organic cathodes for Lithium-ion batteries, Adv. Mater. 37 (2025) 2416661, https://doi.org/10.1002/ADMA.202416661.

[81] S. Li, S. Hu, H. Li, C. Han, Initiating a high-rate and stable aqueous air battery by using organic N-heterocycle anode, Angew. Chem. Int. Ed. 63 (2024) e202318885, https://doi.org/10.1002/ANIE.202318885.

[82] H. Yu, S. Li, J. Yang, Y. Xu, Y. Li, Towards high-performance anthraquinone-derived cathode material for lithium-ion batteries through rational molecular design, Chem. Eng. J. 466 (2023) 143316, https://doi.org/10.1016/J.CEJ.2023.143316.

[83] F. Nourmohammadian, I. Yavari, B. Mohtat, S.Z. Shafaei, Density functional theory study of 9,10-anthraquinone and its structural isomers, Dyes Pigments 75 (2007) 479–482, https://doi.org/10.1016/J.DYEPIG.2006.06.028.

[84] A.W. Bott, The study of multiple Electron transfer reactions by cyclic voltammetry, Curr. Sep. 16 (1997) 61–66.

[85] J. Gonzalez, M. Lopez-Tenes, A. Molina, Non-Nernstian two-Electron transfer reactions for immobilized molecules: a theoretical study in cyclic voltammetry, J. Phys. Chem. C 117 (2013) 5208–5220, https://doi.org/10.1021/JP312621U.

[86] L. Li, X. Tian, D. Meng, M. Collins, J. Wang, R. Patterson, L. Nguyen, X. Yi, Processing, characterization, and impact of Nafion thin film on photonic Nanowaveguides for humidity sensing, Adv. Photonics Res. 3 (2022) 2100181, https://doi.org/10.1002/ADPR.202100181.

[87] J.S. Choi, J.H. Tsui, F. Xu, S.H. Lee, S.K. Sung, H.J. Lee, C. Wang, H.J. Kim, D. H. Kim, Fabrication of Micro- and Nanopatterned Nafion thin films with tunable mechanical and electrical properties using thermal evaporation-induced capillary force lithography, Adv. Mater. Interfaces 8 (2021) 2002005, https://doi.org/10.1002/ADMI.202002005.

[88] J. Liu, Y. Yuan, H. Fang, Y. Xu, W. Sun, S. Chen, Y. Wang, L.P. Lv, Redox-active Tetramino-benzoquinone π–π stacking and H-bonding onto multiwalled carbon nanotubes toward a high-performance asymmetric supercapacitor, ACS Appl. Energy Mater. 5 (2022) 8112–8122, https://doi.org/10.1021/ACSAEM.2C00627.

[89] E. Shanmugasundaram, N.K. Krishnan, M.K. Mani, S. Thambusamy, C.Y. Kuo, M. Govindasamy, Synthesis of nitrogen incorporated carbon sphere (cβ-CD/N-AQ) from supramolecular electroactive inclusion complex (β-cyclodextrin/N-amino anthraquinone) for symmetric supercapacitor application: experimental and computational investigations, Chem. Eng. J. 520 (2025) 165678, https://doi.org/10.1016/J.CEJ.2025.165678.

[90] X.Y. Yuan, W. Bin Zhang, A. Batol, X.Y. Liu, N. Sen Zhou, J. Zhou, J. Feng, J.H. Liu, X.J. Ma, Quinone-based electrode in electrochemical conversion of salinity gradient energy, Chem. Eng. J. 519 (2025) 165103, https://doi.org/10.1016/J.CEJ.2025.165103.

[91] G. Ma, F. Hua, K. Sun, E. Feng, Z. Zhang, H. Peng, Z. Lei, Anthraquinones-modified porous carbon as composite electrode for symmetric supercapacitor, Ionics (Kiel). 24 (2018) 549–561, https://doi.org/10.1007/S11581-017-2215-6.

[92] A. Halder, M. Ghosh, A.M. Khayum, S. Bera, M. Addicoat, H.S. Sasmal, S. Karak, S. Kurungot, R. Banerjee, Interlayer hydrogen-bonded covalent organic frameworks as high-performance supercapacitors, J. Am. Chem. Soc. 140 (2018) 10941–10945, https://doi.org/10.1021/JACS.8B06460.

[93] V. Montes-García, C. Valentini, D. Klymovych, W. KuKułka, L. Shi, V. Patroniak, P. Samorí, A. Ciesielski, Template-assisted synthesis of hollow anthraquinone-based covalent organic frameworks for aqueous zinc-ion hybrid supercapacitors, Chem. Commun. 60 (2024) 9408, https://doi.org/10.1039/D4CC03216K.

[94] Y. Yang, C. Zhang, G. Zhao, Q. An, Z. yuan Mei, Y. Sun, Q. Xu, X. Wang, H. Guo, Regulating the electron structure of covalent organic frameworks by strong electron-withdrawing nitro to construct specific Li+ oriented channel, Adv. Energy Mater. 13 (2023) 2300725, https://doi.org/10.1002/AENM.202300725.